Tectonics

RESEARCH ARTICLE
10.1029/2022TC007291

Analog Models of Lithospheric-Scale Rifting Monitored in an X-Ray CT Scanner

F. Zwaan[1,2] **and G. Schreurs**[1]

[1]Institute of Geological Sciences, University of Bern, Bern, Switzerland, [2]Helmholtz Centre Potsdam - GFZ German Research Centre for Geosciences, Potsdam, Germany

Key Points:

- We present the first-ever lithospheric-scale analog models of rifting monitored in a CT scanner, revealing their complex internal deformation
- We quantify this deformation via Digital Image Correlation analysis, and show the impact of coupling and oblique rifting on rift evolution
- The successful application of our novel modeling approach provides a strong incentive for follow-up tectonic modeling studies

Correspondence to:

F. Zwaan,
frank.zwaan@geo.unibe.ch;
frank.zwaan@gfz-potsdam.de

Citation:

Zwaan, F., & Schreurs, G. (2023). Analog models of lithospheric-scale rifting monitored in an X-ray CT scanner. *Tectonics*, *42*, e2022TC007291. https://doi.org/10.1029/2022TC007291

Received 2 MAR 2022
Accepted 14 DEC 2022

Author Contributions:

Conceptualization: F. Zwaan, G. Schreurs
Data curation: F. Zwaan
Formal analysis: F. Zwaan
Funding acquisition: G. Schreurs
Investigation: F. Zwaan
Methodology: F. Zwaan, G. Schreurs
Project Administration: G. Schreurs
Resources: G. Schreurs
Supervision: G. Schreurs
Validation: F. Zwaan, G. Schreurs
Visualization: F. Zwaan
Writing – original draft: F. Zwaan
Writing – review & editing: F. Zwaan, G. Schreurs

Abstract Rifting and continental break-up are fundamental tectonic processes, the understanding of which is of prime importance. However, the vast temporal and spatial scales involved pose major limitations to researchers. Analog tectonic modeling represents a great means to mitigate these limitations, but studying the complex internal deformation of lithospheric-scale models remains a challenge. We therefore present a novel method for lithospheric-scale rifting models that are uniquely monitored in an X-ray CT scanner, which combined with digital image correlation (DIC) techniques, provides unparalleled insights into model deformation. Our first models illustrate how the degree of coupling between competent lithospheric layers, which are separated by a weak lower crustal layer, strongly impacts rift system development. Low coupling isolates the upper crust from the upper lithospheric mantle layer below, preventing an efficient transfer of deformation between both layers. By contrast, fast rifting increases coupling, so that deformation in the mantle is efficiently transferred to the upper crust, inducing either a symmetric or asymmetric (double) rift system. Furthermore, oblique divergence may lead to en echelon graben arrangements and delayed exhumation of the lower crustal layer. The successful application of our novel modeling approach, yielding these first-order insights, provides a clear incentive to continue running lithospheric-scale rifting models, and to apply advanced monitoring techniques to extract as much information from models as possible. There is indeed a broad range of opportunities for follow-up studies within (and beyond) the field of rift tectonics.

Plain Language Summary The Earth's surface consists of tectonic plates that are in constant motion, driven by titanic forces deep within the planet. One of the key plate tectonic processes is the stretching (rifting) and eventual break-up of continents, leading to the opening of oceanic basins. Understanding the mechanisms involved is of great importance. However, studying continental break-up is challenging due to the vast size of plate tectonic systems, and the extensive timescales over which they evolve: plate tectonic processes can rarely be directly observed. A practical solution to this issue is the use of analog experiments, which reproduce these processes in a matter of hours or days in a modestly sized laboratory. However, a major obstacle that remains is the opacity of these models: similar to tectonic plates, these models are opaque, so that their internal evolution remains hidden. X-ray CT-scanning provides an unrivaled means to reveal a model's internal structures during a model run. Here we present the first-ever application of CT-scanning to monitor relatively complex lithospheric-scale models of continental rifting. The CT scans provide unique insights into the internal evolution of such models, and we point out various possibilities for interesting follow-up studies.

1. Introduction

Rifting and the formation of rifted margins during continental break-up represent a fundamental part of the Wilson cycle (e.g., Wilson, 1966; Wilson et al., 2019). The dynamic evolution of rifts and rifted margins and the processes involved is intensely studied for various reasons. Not only do rifts and rifted margins harbor vast fossil energy reserves (Levell et al., 2010; Zou et al., 2015), they also have great potential for the production of geothermal energy production (e.g., Bonechi et al., 2021; Burnside et al., 2020; Freymark et al., 2017) and potentially natural hydrogen gas (Smith et al., 2005), whereas their sedimentary archives yield crucial insights into past global and climate change (Catuneanu et al., 2009; Catuneanu & Zecchin, 2013; Haq et al., 1987; Kirschner et al., 2010). However, rifts and riftend margins often occur in regions with large concentrations of human population, which are therefore at risk from natural hazards such as volcanism, earthquakes (submarine) landslides and tsunamis (Biggs et al., 2021; Brune, 2016; Gouin, 1979). Hence a thorough understanding of the geological processes that shape rifts and rifted margins is of utmost importance to human society.

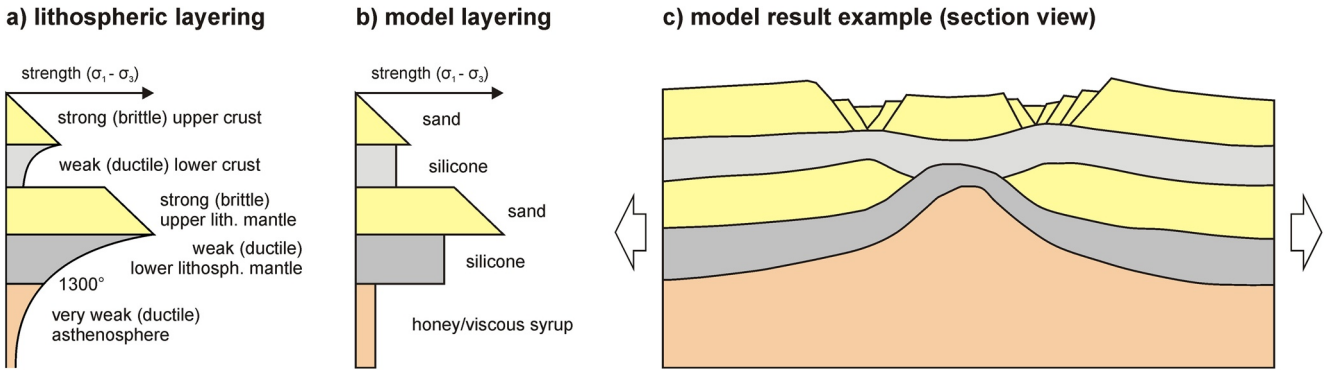

Figure 1. Example of lithospheric-scale rifting model set-up and result in 2D view. (a) Schematic strength profile of a four-layer lithosphere in nature. (b) Analog model materials used to reproduce the natural strength profile in panel (a). (c) Example of a four-layer model result obtained at the end of a model run. Adopted from Zwaan et al. (2019), based on Allemand and Brun (1991).

However, we face various challenges when studying the evolution of rifts and rifted margins. Firstly, these tectonic systems extend over vast areas so that studying them in detail is highly challenging. Furthermore, direct access to rifts and rifted margins is often very limited since large parts of these systems are situated below sea level, and on top of that, are often covered by thick post-rift sedimentary sequences. These challenges have been somewhat overcome through the use of geophysical techniques, especially seismic methods, and the drilling of deep boreholes. However, possibly the most significant and lasting obstacle on our way to understanding rift processes is caused by the long timescales at which they occur, as it is simply not possible to directly observe the development of rift systems over millions of years.

In order to overcome this major obstacle, researchers have since long applied scaled analog models, which allow the simulation of tectonic systems and associated processes that act on vast spatial and temporal scales within a matter of hours or days in a modest laboratory, using relatively simple analog materials at limited financial costs. A large number of analog modeling studies focusing on rift tectonics have been published, and these studies have yielded a wealth of useful insights, as summarized in various reviews and overview papers (Allemand & Brun, 1991; Bahroudi et al., 2003; Beslier, 1991; Brun, 1999, 2002; Brun et al., 2018; Corti et al., 2003; Corti, 2012; Koyi, 1997; McClay, 1990, 1996; Michon & Merle, 2000, 2003; Naylor et al., 1994; Vendeville et al., 1987; Zwaan et al., 2019; Zwaan & Schreurs, 2022).

Of these analog modeling studies, a large part focuses on crustal-scale structures, which is permissible when considering small-scale processes or very early rift stages, but these relatively simple models cannot capture the full rift system. Especially important when considering the full scope of rifting and continental break-up is the influence of the asthenosphere, that is, the isostatic compensation that asthenospheric flow exerts on a rift system. In analog modeling studies that simulate lithospheric-scale rifting in a normal gravity field, the isostatic influence of the asthenosphere is generally simulated with a dense low-viscosity fluid (syrup or honey), on which the model materials representing the lithosphere float (e.g., Allemand & Brun, 1991; Autin et al., 2010, 2013; Benes & Davy, 1996; Benes & Scott, 1996; Beniest et al., 2018; Brun & Beslier, 1996; Capelletti et al., 2013; Molnar et al., 2017, 2018; Nestola et al., 2013, 2015; Samsu et al., 2021; Sun et al., 2009; Figure 1). The rheological layering of lithospheric-scale models in an enhanced gravity field (i.e., centrifuge models) is very similar, although the materials are generally of a higher viscosity in such experiments (e.g., Agostini et al., 2009; Corti, 2008; Corti et al., 2013).

However, all of these previous lithospheric-scale rifting models have an important disadvantage in that the internal model evolution has so far not been monitored and analyzed in real time. Where the internal deformation of crustal-scale models can in some cases be partly observed via a glass sidewall (while accounting for boundary friction effects), the internal deformation of lithosphere-scale models remains elusive since the model lithosphere generally contains different (sticky viscous) layers that hamper direct observation of the model interior through glass. These viscous layers also hamper the use of surface structures and topography (including the topography of the base of the lithosphere, e.g., Nestola et al., 2013, 2015) as reliable indicators for internal deformation since these layers often decouple internal model deformation from the surface structures (e.g., Allemand et al., 1989; Molnar et al., 2017, 2018; Zwaan et al., 2019, 2021; Zwaan, Chenin, et al., 2022; Figure 1). Sectioning is another

option to gain insight into a model's interior, but this is a destructive method that can only be used to interpret the model evolution through the reconstruction of markers, and only after completion of the model (e.g., Beslier, 1991; Brun & Beslier, 1996). Furthermore, sectioning of lithospheric-scale models containing various viscous layers is often a challenging task since the models are highly unstable and deform easily while making the sections. The same goes for removing the crustal layers to scan the topography of the base of the crust after the model run (Nestola et al., 2015).

So far the only reliable non-destructive method to truly peek into otherwise opaque analog models materials during an experimental run is X-ray CT-scanning (e.g., Colletta et al., 1991, Sassi et al., 1993; Schmid et al., 2022a, 2022b; Schreurs et al., 2003; Holland et al., 2011; Zwaan, Schreurs, & Adam, 2018). This technique, which basically relies on the visualization of density differences within the model materials (e.g., induced by layering and dilatation along faults) has been around for a number of decades and has been applied in various studies to analyze crustal-scale rifting models (e.g., Schmid et al., 2022a, 2022b; Zwaan et al., 2016, 2020; Zwaan, Schreurs, & Adam, 2018). Yet to our knowledge CT-scanning has so far never been used to analyze the much more complex deformation in lithospheric-scale models, providing a strong incentive to push forward the state of the art in modeling.

The aim of this paper is therefore to present the unique possibilities of a newly designed analog model set-up for studying lithospheric-scale rifting, which allows for the first time the monitoring of model-internal deformation via X-ray CT scanning methods. The resulting CT imagery does not only allow a qualitative assessment of internal model evolution, but we can even quantify strain within the model through the use of digital image correlation (DIC) techniques normally applied for strain analysis of model surfaces. Furthermore, next to simple orthogonal rifting our new set-up enables us to simultaneously simulate lateral movements as well, opening many possibilities for simulating different tectonic regimes such as oblique extension and (oblique) basin inversion. The results from four rifting models presented in this paper demonstrate the general viability and potential of this new modeling procedure.

2. Methods

2.1. Materials

Similar to previous analog modeling studies of lithospheric-scale rifting (e.g., Allemand & Brun, 1991; Brun & Beslier, 1996; Nestola et al., 2015; Figure 1), we apply both brittle and viscous materials to simulate the brittle and ductile parts of the lithosphere, as well as the asthenosphere (Figure 2c). Assuming a stable four-layer continental lithosphere prior to deformation, the model consists from top to bottom of a strong (brittle) upper crust (UC), a (weak) ductile lower crust (LC), a strong (brittle) upper lithospheric mantle (ULM), a weak (ductile) lower lithospheric mantle (LLM) and a very weak (ductile) asthenosphere with the following relative thicknesses of the lithospheric layers from top to bottom: 2:1:1.5:2 (Figure 2c and Table 1).

For both the brittle upper crust and brittle upper mantle layer, we use FS900S feldspar sand produced by Amberger Kaolinwerke (https://www.quarzwerke.com) (Table 1). This angular feldspar sand as provided by the company has a dominant grain size between 100 and 250 μm (65% of grains, see grain size distribution in Willingshofer et al., 2018). In contrast to other modeling studies (e.g., Beniest et al., 2018), we do not have the means to sieve and remove the fine fraction of this FS900S sand to the 100–250 μm range prior to use. However, new ring shear tests completed at GFZ Potsdam show that not removing the finer fraction of the feldspar sand does not significantly affect the internal friction angle (Zwaan, Schreurs, et al., 2022). The density of the feldspar sand is ca. 1,300 kg/m^3 when added into the model by means of sieving from a height of ca. 30 cm.

The ductile lower crust and ductile lower lithospheric mantle are simulated using viscous mixtures of SGM-36 silicon oil (Polydimethylsiloxane or PDMS) formerly produced by Dow Corning, now part of Dow Chemical (www.dow.com), and F120 corundum sand acquired from Carlo AG (www.carloag.ch) (Table 1). The PDMS has a bulk density of 965 kg/m^3 (Rudolf et al., 2016), whereas the corundum grains in the corundum sand have a bulk density of 3,950 kg/m^3. The grain size of the corundum sand lies between 88 and 125 μm. By mixing these components in different ratios, we obtain viscous materials with different (near-Newtonian) rheology and varying densities. We use a mixture with a density of ca. 1,300 kg/m^3 and a viscosity of 6×10^4 Pa·s (viscous mixture 1) to simulate the lower crust, while a mixture with a density of ca. 1,400 kg/m^3 and a 8×10^4 Pa·s (viscous mixture 2) for the lower lithospheric mantle (Zwaan, Schreurs, Ritter, et al., 2018; Table 1).

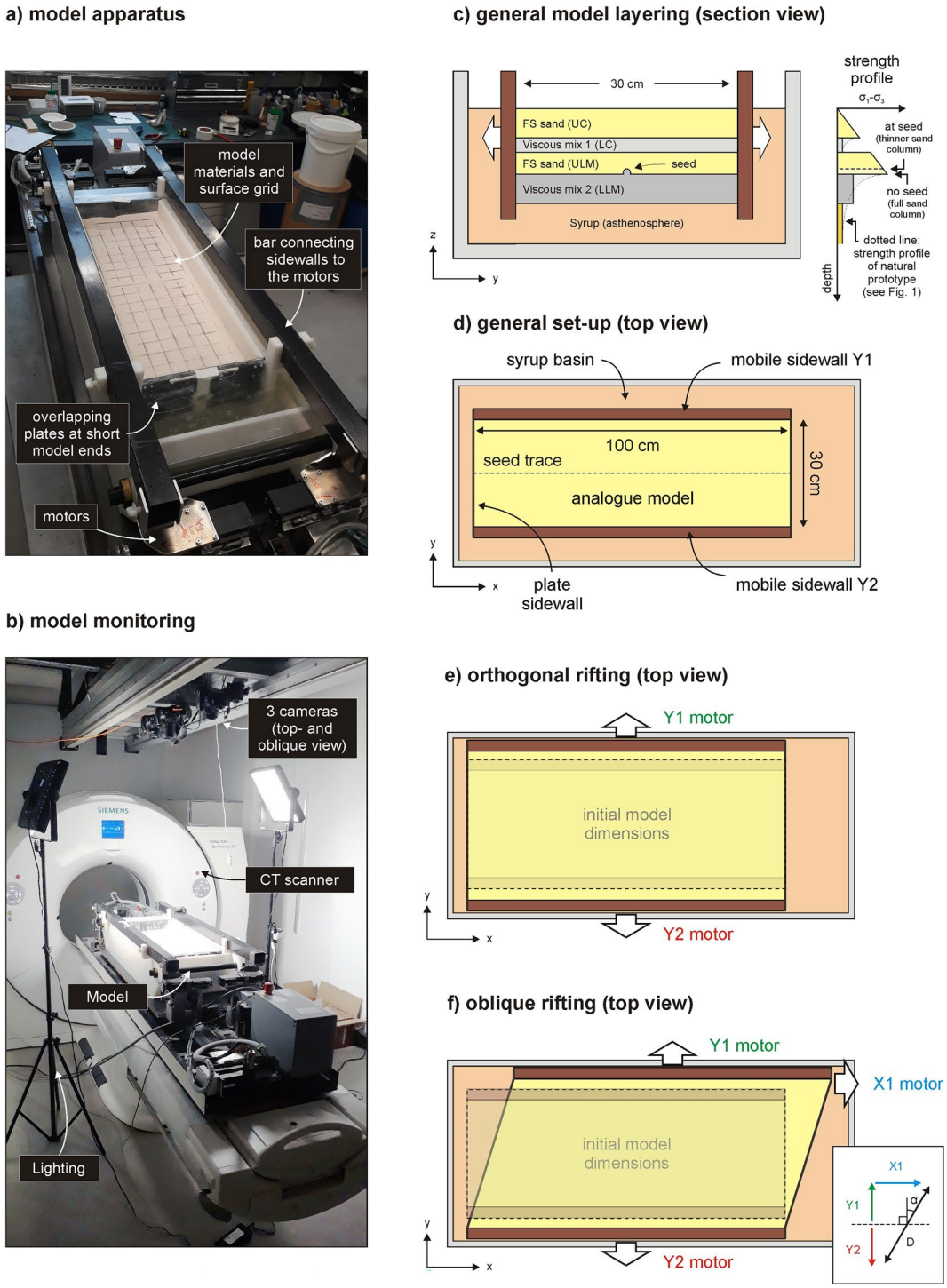

Figure 2. Model set-up. (a) The NAMAZU model apparatus with the different components of our new set-up and their links to the various motors. (b) Model run in the CT scanner with the model, camera rig, lighting and the CT scanner itself indicated. The model runs in 15 min intervals, after which it is halted and moved into the CT scanner to obtain CT slices perpendicular to the long axis of the model. (c) Schematic cross-section of the model set-up depicting the model layering and the space for the syrup to move below the inner sidewalls for isostatic compensation. FS: feldspar sand, UC: upper crust, LC: lower crust, ULM: upper lithospheric mantle, LLM: lower lithospheric mantle. On the right: schematic strength profile of the model layering and its natural equivalent (compare with Figure 1). (d) Schematic top view of the model set-up prior to deformation. (e, f) Schematic top view of model deformation and the motors (Y1, Y2 and X1) involved: (e) orthogonal rifting, and (f) oblique rifting, where the divergence direction (α) is defined as the angle between the divergence direction and the normal to the model axis. Total divergence at a given point in time (*D*) is the combined motion of the motors, measured in the divergence direction.

Table 1
Material Properties

Granular materials	Feldspar sand[a]	Liaver beads[b]
Represents	Upper crust and upper lithospheric mantle	-
Grain size range (ϕ)	100–250 μm	100–300 μm
Density (sieved) (ρ_{sieved})	ca. 1,300 kg/m^3	ca. 530 kg/m^3
Internal peak friction angle (φ_p)	35.0°	36.0°
Dynamic-stable friction angle (φ_d)	29.9°	28.6°
Reactivation friction angle (φ_r)	32.0°	30.1°
Cohesion (C)	51 Pa	0 Pa

Viscous materials	Pure PDMS[c]	Viscous mixture 1[d]	Viscous mixture 2[d]	Glucose syrup[e]
Represents	-	Lower crust	Lower lith. Mantle	Asthenosphere
Weight ratio PDMS: corundum sand	-	1 : 0.52	1 : 0.7	-
Density (ρ)	965 kg/m^3	ca. 1,300 kg/m^3	ca. 1,400 kg/m^3	ca. 1,450 kg/m^3
Viscosity[f] (η)	ca. 2.8·10^4 Pa·s	ca. 6·10^4 Pa·s	ca. 8·10^4 Pa·s	ca. 65 Pa·s
Rheology[g]	Newtonian (n = 1)	near-Newtonian (n = 1.05–1.10)	near-Newtonian (n = 1.05–1.10)	near-Newtonian (n = ca. 1.09)

[a]Feldspar sand properties after Zwaan, Schreurs, et al. (2022). [b]Liaver beads properties after Warsitzka et al. (2019). [c]Pure PDMS rheology after Rudolf et al. (2016) and Zwaan, Schreurs, Ritter, et al. (2018). [d]Rheology of viscous mixtures 1 and 2 after Zwaan, Schreurs, Ritter, et al. (2018). [e]Glucose syrup rheology after Schmid et al. (2022c). [f]Viscosity value holds for model strain rates <10^{-4}/s. [g]Power-law exponent n (dimensionless) represents sensitivity to strain rate.

These four layers representing the lithosphere float on top of a Glucosweet 44 glucose syrup layer simulating the asthenosphere (Figure 2c and Table 1). This viscous glucose syrup is acquired from ADEA (https://www.adea-srl.it/) and has a density of ca. 1,450 kg/m^3. The higher density of the syrup with respect to the overlying model materials prevents the latter materials from sinking into the syrup. Rheometer test performed at University of Roma TRE show that the syrup has a near-Newtonian rheology with a relatively low viscosity of ca. 65 Pa·s, when compared to the viscosity of 8 × 10^4 Pa·s of the lowermost viscous layer (Schmid et al., 2022c; Zwaan, Schreurs, Ritter, et al., 2018; Table 2). This viscosity difference is representative of the viscosity difference between the lithosphere and asthenosphere in nature (Figures 1 and 2c).

In order to mark layering (both within sand layers, as well as between brittle and viscous layers) on CT imagery (Section 2.4), we add thin layers (≤1 mm) of "Liaver beads," that is, foamed glass beads produced by Liaver (www.liaver.com) (grain size between 100 and 300 μm, density = ca. 530 kg/m^3, Warsitzka et al., 2019). The Liaver beads have very different X-ray attenuation coefficients with respect to the other analog model materials and clearly stand out on CT images. Since the Liaver beads have similar internal friction angles as the feldspar sand (Table 1), and are only used as thin layers within brittle model materials or to mark the transition between the syrup and the lower viscous layer, their use is not considered to have any major impact on model deformation.

Table 2
Model Parameters

Model	Seed		Divergence direction (angle α)[a]	Velocity (Y1 + Y2)[b]	Velocity (X1)[b]	Effective divergence velocity	Model duration	Total divergence (D) (at angle α)	CT-scanned
A[c]	No		0°	10 mm/hr	0 mm/hr	10 mm/hr	150 min	25 mm	Yes
B[d]	Yes		0°	10 mm/hr	0 mm/hr	10 mm/hr	240 min	40 mm	-
C	Yes		0°	10 mm/hr	0 mm/hr	10 mm/hr	300 min	50 mm	Yes
D[e]	Yes	Phase 1:	45°	7.2 mm/hr	7.2 mm/hr	10 mm/hr	195 min	32.5 mm	Yes
		Phase 2:	45°	21.6 mm/hr	21.6 mm/hr	30 mm/hr	105 min	52.5 mm	Yes

[a]See definition of angle α in Figure 2f. [b]See definition of Y1, Y2 and X1 in Figures 2d–2f. [c]Half the standard layer thickness used (see Section 2.3). [d]Technical issues: parts of time-lapse imagery missing (break between t = 75 min and t = 180 min). [e]Total model duration: 300 min; total divergence: 85 mm.

2.2. Set-Up

The general modeling set-up principle is similar to that of previous analog models of lithospheric-scale rifting with a lithosphere floating on a heavy fluid, with the exception that our set-up specifically allows for oblique rifting and X-ray CT-scanning (Figures 1 and 2). Our new lithospheric-scale modelling set-up is based on a conceptual design by Zwaan (2017) and has been constructed by engineers from IPEK, Ostschweizer Fachhochschule in Rapperswil, Switzerland. It includes a number of components that are added to the highly versatile NAMAZU machine, also developed by IPEK, which has been used for various previous analog modeling studies at the Tectonic Modeling Laboratory of the Institute of Geological Sciences at the University of Bern, Switzerland (e.g., Alonso-Henar et al., 2015; Fedorik et al., 2019; Klinkmüller, 2011; Schori et al., 2021; Zwaan et al., 2016, 2020, 2021; Zwaan, Chenin, et al., 2022; Zwaan, Schreurs, Adam, 2018).

Our new set-up includes a large basin containing the glucose syrup and is installed on the NAMAZU machine (Figure 2). A rectangular framework of inner sidewalls that contain the materials representing the model lithosphere is hung down in this basin (Figures 2a and 2c). These inner sidewalls are fixed to bars that on their turn are connected to computer-controlled motors. Motors Y1 and Y2 can induce orthogonal extension of the model materials contained within the inner framework, or, in combination with simple-shear motion (imposed by motor X1), can produce oblique rifting (Figures 2d–2f). The direction of (oblique) rifting is defined as angle α, which is the angle between the normal to the long model axis and the combined motion directions of the motors (Figure 1f). Importantly, as the model is deforming, the syrup can freely flow below the inner model sidewalls, allowing for isostatic compensation at the base of the simulated lithosphere that analog models with a fixed base lack (e.g., Zwaan et al., 2019). The short inner sidewalls are equipped with hinges and consist of overlapping plates to accommodate the (oblique) rifting applied in the models, while still containing the model materials representing the lithosphere within the inner framework (Figures 2a and 2f). Importantly, the experimental set-up is constructed from X-ray transparent materials that allow for optimal X-ray CT-scanning.

2.3. Model Preparation and Parameters

Preparing the models involves a number of steps including freezing of the syrup to stabilize the model materials during model construction. All steps are described in detail in the supplementary material (i.e., in a GFZ data publication by Zwaan & Schreurs, 2023b). The details of the four models completed for this study are provided below and in Table 2. It may be noted that the models presented in this study do not represent a full systematic study, but rather aim to explore the potential provided by our new modeling approach.

Model A serves as a reference model. It involves orthogonal rifting and the total lithospheric thickness is half that of the subsequent models (i.e., the thicknesses of the upper crust, lower crust, upper lithospheric mantle and lower lithospheric mantle were 10, 5, 7.5 and 10 mm, respectively). The model does not contain any structural inheritance to localize deformation under the standard divergence velocity (10 mm/hr). The total model duration amounts to 150 min for a total of 25 mm of divergence, and the model is CT-scanned.

Model B and C also involve orthogonal rifting at the same standard divergence velocity as Model A, but have a standard model thickness of 20, 10, 15 and 20 mm for the upper crust, lower crust, upper lithospheric mantle and lower lithospheric mantle, respectively. Another contrast to Model A is the insertion of a weakness or "seed," a rod of viscous material at the base of the brittle upper lithospheric mantle layer that runs along the whole length of the model, to localize deformation. Such seeds have been used in various previous modeling studies to simulate linear weaknesses such as crustal shear zones (e.g., Le Calvez & Vendeville, 2002; Osagiede et al., 2021; Schmid et al., 2022a, 2022b; Zwaan et al., 2016, 2021; Zwaan, Chenin, et al., 2022), but we apply them in the modeled upper lithospheric mantle instead (Figure 1c). Furthermore, Model B undergoes a total of 40 mm of divergence over a 4-hr period, where Model C, which is a rerun of Model B in the CT scanner, undergoes and extra hour of deformation for a total of 50 mm of divergence.

Finally, CT-scanned Model D involves the same standard layering as Models B and C, but initially undergoes $\alpha = 45°$ oblique rifting at the standard divergence velocity of 10 mm/hr for the first 195 min (32.5 mm of divergence). Subsequently, the divergence velocity is tripled to 30 mm/hr for the remaining 105 min of the model run, covering an additional 52.5 mm of divergence, so that the total divergence amounts to 85 mm.

2.4. Scaling

Applying analog modeling scaling laws (e.g., Hubbert, 1937; Ramberg, 1981; Weijermars & Schmeling, 1986) demonstrates the suitability of our models for simulating continental rifting processes (detailed scaling calculations can be found in Appendix A). Specifically, the (standard) models have a geometric scaling ratio of $6.7 \cdot 10^{-7}$, so that 1 cm corresponds to 15 km in nature, and our 6.5 thick lithospheric layering represents a ca. 100 km thick lithosphere in nature. The standard divergence velocity in our Models B, C and D (10 mm/hr) translates to 2.6–3.1 mm/yr in nature, whereas the faster velocity in the second phase of Model D (30 mm/hr) translates to 7.8–9.3 mm/yr in nature. The 10 mm/hr divergence in Model A, which has a thinner simulated lithosphere, amounts to 10.6–12.4 mm/yr. These values are close to plate divergence velocities observed in natural rift systems (e.g., the East African Rift, Saria et al., 2014), and also dimensionless scaling ratios are very similar between model and nature, demonstrating that scaling requirements are fulfilled (Appendix A).

2.5. Model Monitoring and Analysis

We use various techniques to monitor and analyze our models and the deformation they undergo. Firstly, we use a rig containing three high-resolution 36.3 megapixel D810 Nikon cameras, one of which provides top view images, and the other two inclined (stereoscopic) images of the model surface (Figure 2b). These cameras are computer-programmed to take pictures every 30 s, creating time-lapse series. At the same time, we apply a timer for the lighting on one side of the model to switch on and off every 30 s, so that we obtain two time series, of images with and without shade (each with 1 min intervals). Note that we apply a thin <1 mm thick, 4 × 4 cm surface grid made of corundum sand to highlight surface deformation and we sprinkle coffee powder on the surface for optimizing DIC analysis.

The time series images with shade provide visual clues about surface deformation evolution, whereas the time series images without shade are ideal for 2D (map view) displacement and strain analysis. This strain analysis is done using digital image correlation (DIC) DaVis 10.1 software from LaVision (www.lavision.de), which compares surface patterns on images (if needed after correction for their inclination) from different time steps and detects horizontal surface displacements (displacement vectors) (e.g., Adam et al., 2005; Boutelier et al., 2019). The result is a detailed and quantified analysis of surface model deformation over time, which we use in particular for generating incremental and cumulative maximum normal strain (MNS) data. These maximum normal strain data represent the deformation of the longest axis of the strain ellipse, and serves as a proxy for extensional deformation (Schmid et al., 2022a, 2022b; Zwaan et al., 2021; Zwaan, Chenin, et al., 2022).

Furthermore, the inclined images, preferably without shade, allow for stereoscopic reconstruction of the model topography over time through Agisoft Photoscan photogrammetry software (www.agisoft.com) (e.g., Maestrelli et al., 2020). By comparing the different distortions of the images from the stereoscopic cameras, the software can reconstruct the 3D model surface for selected time steps. These 3D surfaces are georeferenced using markers with known locations placed on the model set-up, to produce properly georeferenced digital elevation models (DEMs) over time. These DEMs are subsequently post-processed in QGIS (www.qgis.org), an open source geographic information system (GIS) software.

Next to 3D photography and the quantitative surface analyses it enables, the key innovation in terms of model monitoring and analysis in our study is the application of X-ray CT-scanning techniques (e.g., Colletta et al., 1991; Holland et al., 2011; Sassi et al., 1993; Schmid et al., 2022a, 2022b; Schreurs et al., 2003; Zwaan, Schreurs, & Adam, 2018, Figure 2b), allowing for the first time to directly trace the internal 3D structural evolution of this type of models. The X-ray CT-scanning of Models A, C and D is done in the 64 slice Siemens Somatom Definition AS apparatus at the Institute of Forensic Medicine of the University of Bern. For practical reasons, the central 50 cm area is selected for CT-scanning in all of the scanned models. Scanning intervals are 15 min, each representing 2.5 mm of divergence under standard divergence velocities, and 7.5 mm of divergence under the high divergence velocity in the second phase of Model D. The CT data are subsequently visually analyzed in Horos (https://horosproject.org/), an open source DICOM viewer software. This analysis involves the tracing of internal deformation, but also of model topography and internal model layer evolution.

Finally, vertical CT section time series from selected transects in orthogonal rifting Models A and C are used for 2D DIC analysis in DaVis, providing the first-ever truly quantified insights into internal deformation of analog models of lithospheric-scale rifting. This analysis is done on time series of vertical CT sections on which, similar

as done for model surface imagery, displacements are traced. We extract horizontal and vertical in-section (y- and z-) displacements, as well as vorticity data. This vorticity data indicates the degree to which displacements deviate from the nearby displacement field, revealing in-section displacement along faults and shear zones.

3. Results

3.1. Orthogonal Rifting Model A

The orthogonal rifting model A involves a simulated lithosphere with half the standard thickness and no seed in the upper mantle layer (see Section 2.3). Results of this model, which is stretched at a divergence velocity of 10 mm/hr during 150 min, are presented in Figure 3. Topography analysis (Figures 3a and 3b) reveals the development of significant boundary effects in the shape of (half-)grabens along the longitudinal sidewalls, whereas no surface deformation is visible in the center of the model. Furthermore, these boundary effects are strongest toward the mid-point of the longitudinal sides.

The same general pattern of deformation is shown by the results of the DIC analysis (Figures 3c and 3d). The cumulative maximum normal strain data (Figure 3c) highlights that normal faulting is most active along the sidewalls, as is horizontal displacement, which is illustrated by the cumulative horizontal displacement data (Dy in Figure 3d). These Dy data in Figure 3d also reveal that the regions immediately adjacent to the short ends of the model, close to where the short overlapping sidewalls moved apart, undergo some displacement. A further indication of this differential displacement is provided by the slight warping of the surface grid, visible in the background of the DIC results (Figures 3c and 3d).

CT imagery provides additional insights into the internal development of Model A (Figures 3e and 3f). The layering within the simulated lithosphere is not readily visible, but the transition between the model lithosphere and model asthenosphere can be visualized (Figure 3e). The final stage CT section of Model A reveals the boundary effects normal faulting along the longitudinal sidewalls within the model lithosphere, and the rising of the model asthenosphere (Figure 3f).

3.2. Orthogonal Rifting Model B

Model B involves a standard lithosphere thickness, contains a seed in the upper lithospheric mantle layer, and is stretched at a rate of 10 mm/hr over a period of 4 hr (Figure 4). We analyze the model topography and surface deformation only, since the model is not CT-scanned.

The results from the topography analysis show how the model, in stark contrast to Model A (which lacked a seed), starts developing a slight central depression at the surface at about 60 min of deformation (Figure 4b). After 75 min of deformation, two graben structures start to appear at the short ends of the model (Figure 4c). At this point in time, technical issues with the camera rig prevented the acquisition of time-lapse imagery for ca. 90 min, hence subsequent topography data are only available from $t = 180$ min on (Figure 4d). These topography data show the presence of a double graben system, flanking a central depression, as well as some deformation (boundary effects) along the longitudinal sidewalls. Both grabens are well developed, and their combined surface expression is fairly symmetrical, and remains so until the end of the model run (Figure 4e).

The incremental normal strain data obtained from DIC analysis highlights normal faulting over the preceding 5 mm of divergence and reveals that the double graben system seen at $t = 75$ min in the topography analysis results (Figure 4c) is in fact already established at $t = 60$ min, and is initially somewhat better developed near the short ends of the model (Figure 4h). The vectors displaying horizontal displacement in the DIC maps show that the central depression between the double grabens remains in place during the model run, whereas the materials on both side of the double graben system move steadily outward (Figures 4f–4j).

3.3. Orthogonal Rifting Model C

The topography and DIC analysis results from Model C, which is a rerun of Model B monitored in the CT scanner (with 60 min extra runtime), are presented in Figure 5. In addition to CT-scanning, we also perform the same topography and DIC analysis on Model C as done for Model B, allowing for a direct comparison between both models (Figures 4 and 5). Furthermore, we use the CT imagery for a qualitative assessment of model-internal

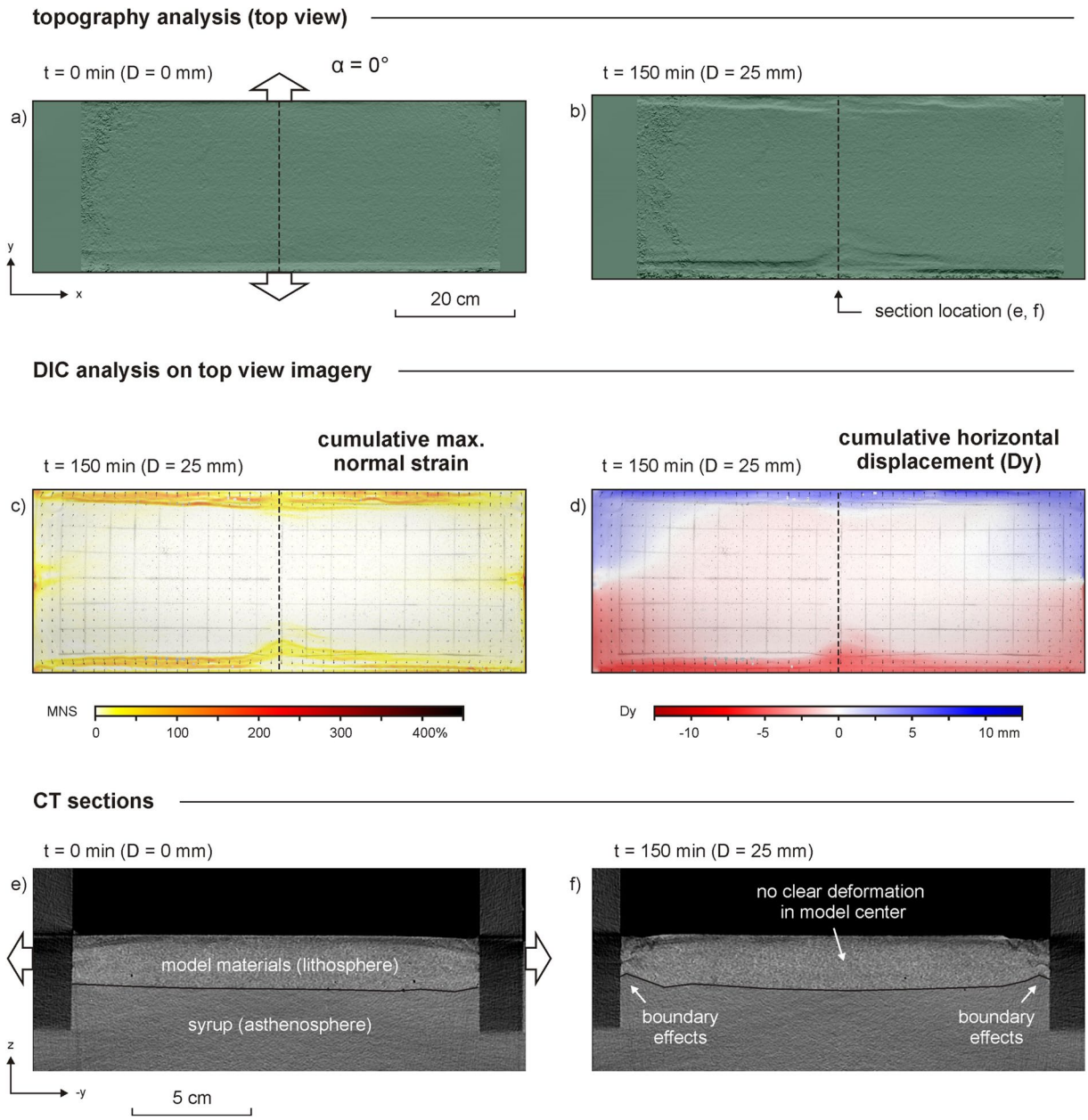

Figure 3. Overview of results from Model A, with a modeled lithosphere of half the standard thickness and no seed, which underwent 10 mm/hr of orthogonal divergence over a period of 150 min. D: total divergence (for definition see Figure 2f). (a, b) Topography analysis results, lighting from top. (c, d) Digital image correlation (DIC) analysis. (c) Cumulative maximum normal strain (MNS) at the end of the model run, representing the length of the longest axis of the strain ellipse in the horizontal plane, which is taken as a proxy for extensional deformation. (d) Cumulative horizontal displacement along the *y*-axis (Dy, parallel to the divergence direction at the end of the model run). (e, f). CT analysis on vertical sections (e) $t = 0$ min, and (f) $t = 150$ min. Section location is indicated in (a–d).

deformation (Figures 6 and 7), as well as for a quantification of internal deformation through DIC analysis on selected CT sections (Figure 8).

3.3.1. Topography and Model Surface DIC Analysis

The topography analysis of Model C reveals a similar surface structure evolution as in Model B (Figures 4a–4e and 5a–5e), with an initial central depression forming, followed by the development of grabens flanking this central depression. Like in Model B, the grabens are initially best developed toward the short ends of the model, before covering the whole length of the model (Figures 4c–4e and 5c–5e). A major difference with Model B, however, is that the double graben arrangement in Model C is highly asymmetric nearer to the short ends of

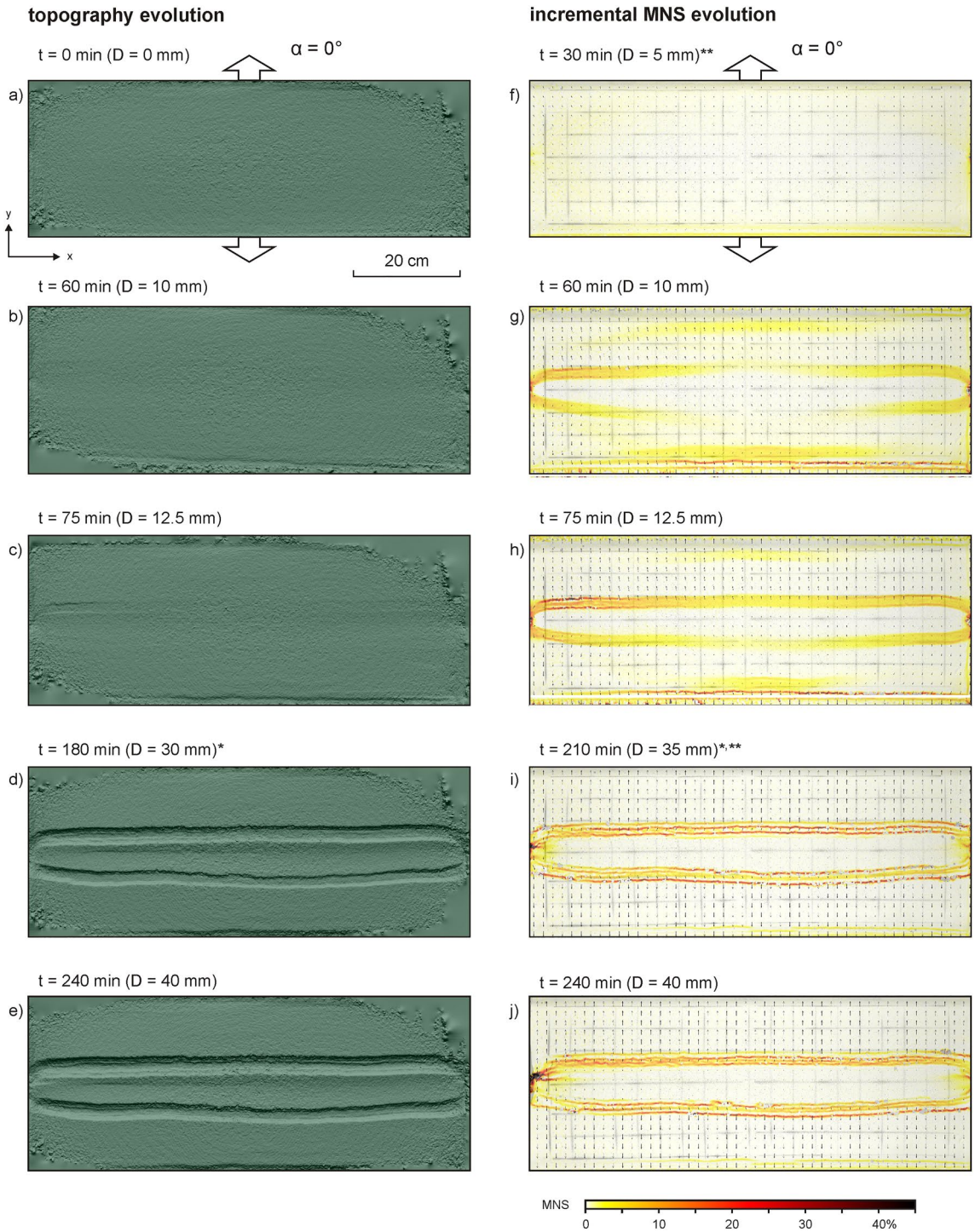

Figure 4. Topography and digital image correlation (DIC) analysis of Model B (orthogonal rifting at a divergence velocity of 10 mm/hr). D: total divergence (for definition see Figure 2f). (a–e) Topography analysis results, lighting from top. (f–j) DIC (incremental MNS [maximum normal strain]) analysis, representing the length of the longest axis of the strain ellipse in the horizontal plane, which is taken as a proxy for extensional deformation. *Due to technical issues, no intermediate data were available between $t = 75$ min and $t = 180$ min **Due to DIC analysis requirements (an initial and deformed state is needed, and the analysis steps in this study are standardized to 5 mm of displacement), $t = 30$ min and $t = 210$ min are the first available data point at the start of the model, and after the data gap, respectively.

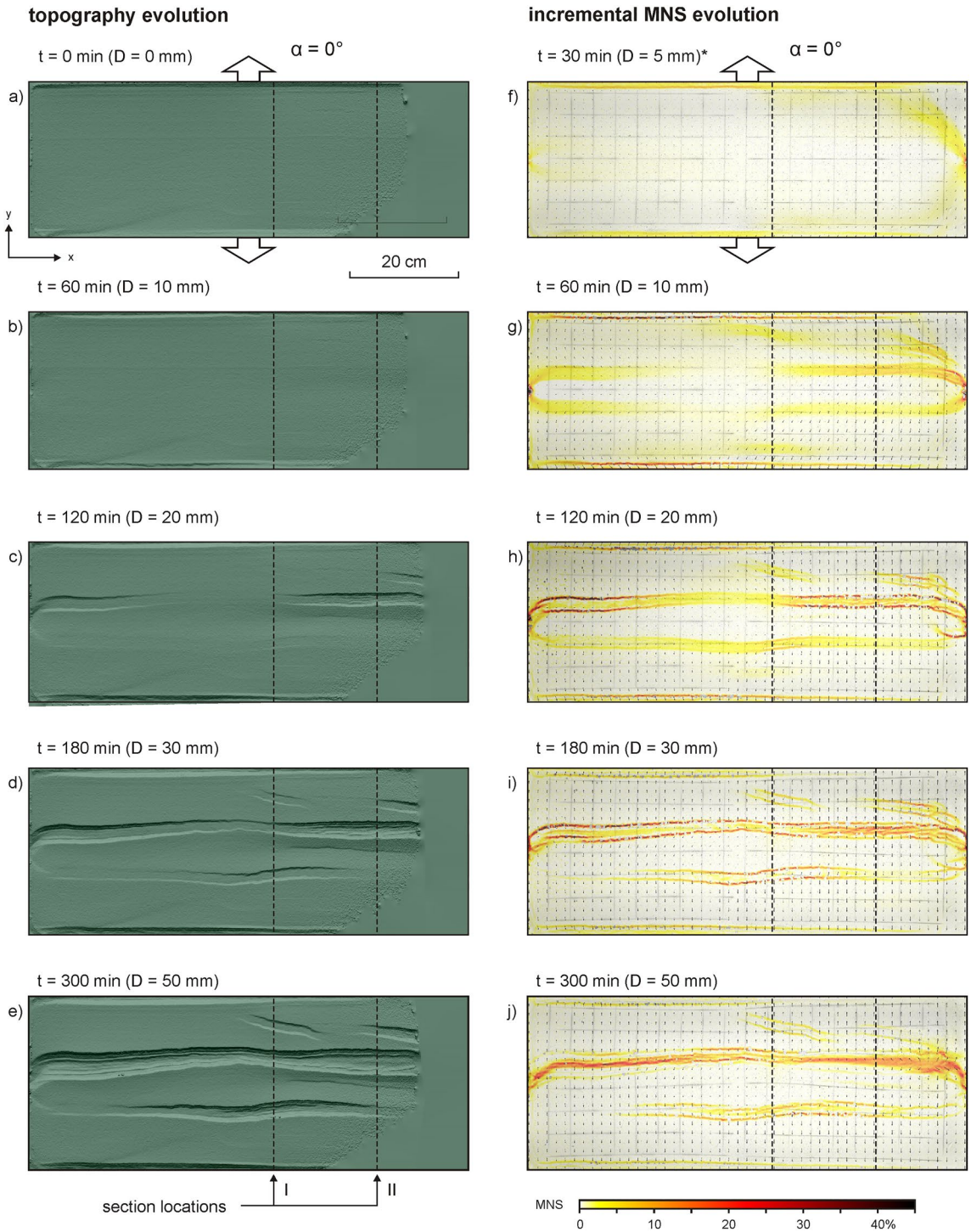

Figure 5. Topography and digital image correlation (DIC) analysis of Model C, which is a (60 min longer) rerun of Model B (orthogonal rifting at a divergence velocity of 10 mm/hr) completed in a CT scanner. D: total divergence (for definition see Figure 2f). (a–e) Topography analysis results, lighting from top. (f–j) DIC (incremental MNS [maximum normal strain]) analysis, representing the length of the longest axis of the strain ellipse in the horizontal plane, which is taken as a proxy for extensional deformation. *Due to DIC analysis requirements (an initial and deformed state is needed, and the analysis steps in this study are standardized to 5 mm of displacement), $t = 30$ min is the first available data point after the start of the model run.

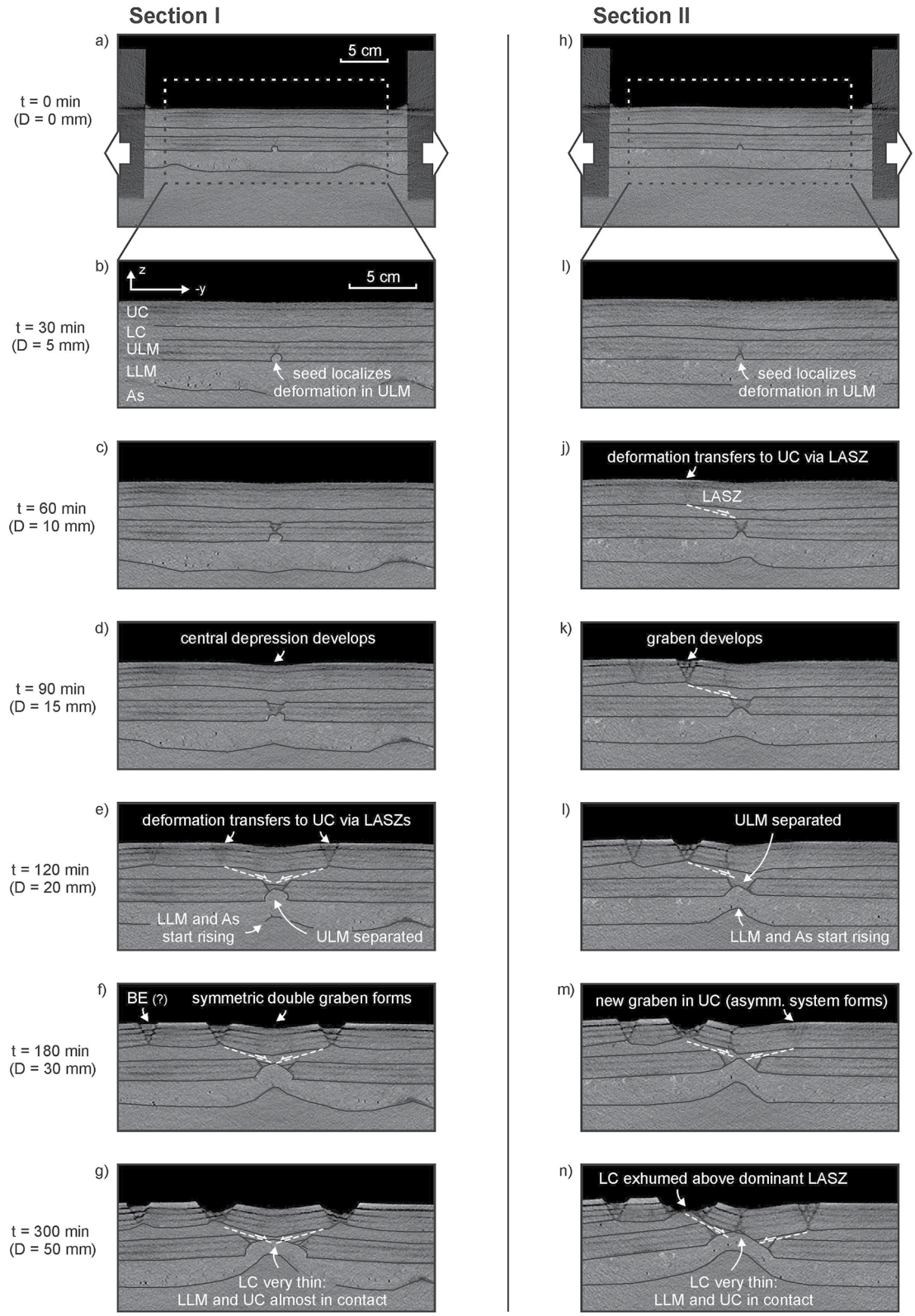

Figure 6. CT sections I and II depicting the internal evolution of the symmetric and asymmetric double rift systems found in Model C, respectively. D: total divergence (for definition see Figure 2f). Dark lines are added to highlight layer contacts. BE: boundary effect, As: asthenosphere, LASZ: low-angle shear zone, LC: lower crust, LLM: lower lithospheric mantle, ULM: upper lithospheric mantle, UC: upper crust. CT section locations are indicated in Figure 5.

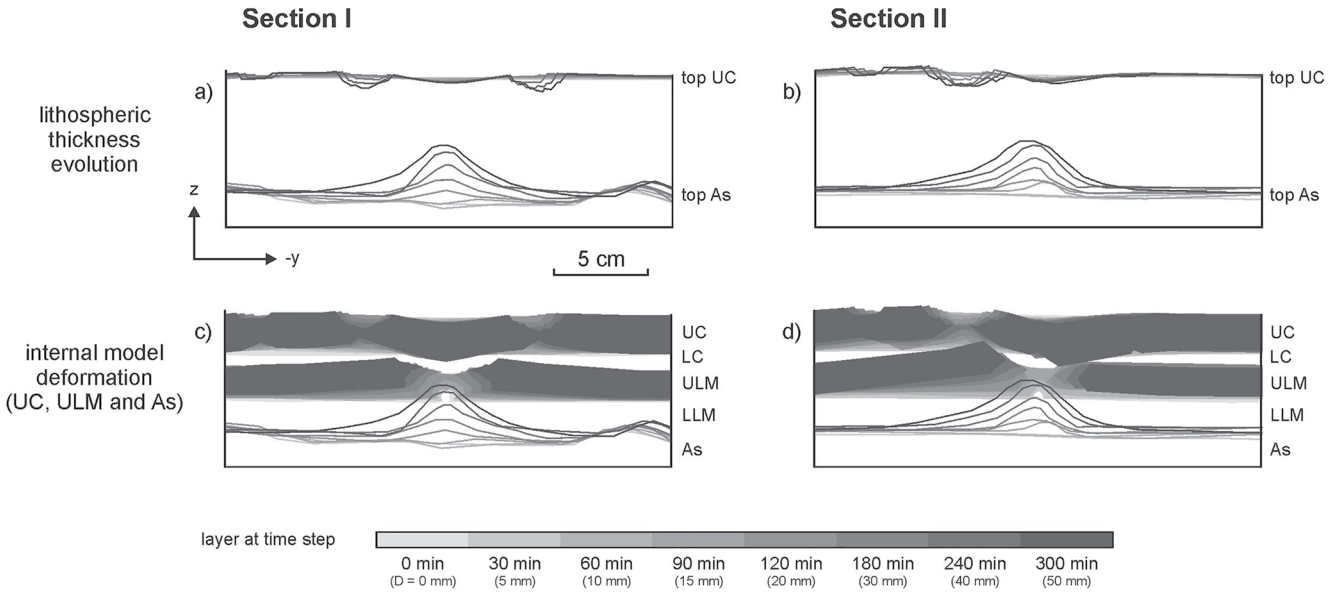

Figure 7. Analysis of the internal evolution of symmetric and asymmetric rift structures seen on CT sections I and II from Model C (Figure 6), respectively. D: total divergence (for definition see Figure 2f). UC: upper crust, LC: lower crust, ULM: upper lithospheric mantle, LLM: lower lithospheric mantle, As: asthenosphere. (a, b) Horizon profiles charting the evolution of the model topography and the top of the asthenosphere layer. (c, d) Horizon profiles charting the evolution of the various layers in the lithosphere. Section locations are indicated in Figure 5.

the model (compare Figures 4c–4e and 5c–5e). At the end of the model run both grabens in the central area of Model C are about equally well developed with the upper graben accounting for the bulk of topography change toward the short ends of the model (Figure 5e). Furthermore, some slight boundary effects are visible along the longitudinal sidewalls, as well as in the upper right corner of the model where some small additional grabens appear (Figure 5e).

Similar to Model B, the DIC results of Model C shows how normal faulting starts localizing before structures are visible at the surface (at $t = 60$ min, Figures 4b, 4g and 5b, 5g). The normal faulting initiates at the short ends of the model before growing toward the model center, and is in fact rather symmetrical in the earlier stages of model evolution (Figure 5g). Only later on, parts of the lower graben are abandoned so that the upper graben could become the dominant structure at the model surface (Figures 5h–5j). The DIC results highlight that the bulk of deformation is accounted for by the grabens along the model's central axis (Figures 5f–5j). The additional grabens in the upper right corner, as well as the boundary effects along the longitudinal sidewall, which are well visible on topography data (Figure 5e), are shown to only localize minor amounts of normal faulting (Figures 5f–5j). An important detail is indicated by the displacement arrows: the central area between the double grabens is only (nearly) stationary (i.e., no vectors visible) where this area is flanked by two active grabens (Figures 5f–5j).

3.3.2. CT Analysis

The acquisition of CT imagery and additional DIC analysis on CT sections allows us to analyze the internal model evolution of Model C (Figures 6 and 7), with an emphasis on the differences between the symmetric and asymmetric rift structures previously identified by the topography and DIC analysis (Sections I and II, respectively, locations of which are shown in Figure 5).

Section I, taken near the center of Model C (Figure 5), shows the development of a symmetric double rift structure (Figures 6a–6g, and 7a, 7c). In the earliest stages of rifting ($t = 30$ min, Figure 6a), the seed in the simulated upper lithospheric mantle layer localizes deformation. As rifting progresses, this leads to the development of a graben structure in the upper lithospheric mantle with a central depression at the model surface (Figures 6c, 6d, and 7c). We subsequently observe the development of two upper crustal grabens flanking this central depression, which are linked to the graben in the upper lithospheric mantle layer by low-angle shear zones (LASZs) in the simulated lower crust (Figures 6e and 7c). At this point in time ($t = 120$ min), the upper lithospheric mantle layer is split in two parts, and also a minor graben forms away from the central double graben structure (Figure 6e). As rifting proceeds, this minor graben does not develop significantly, in contrast to the continuously developing

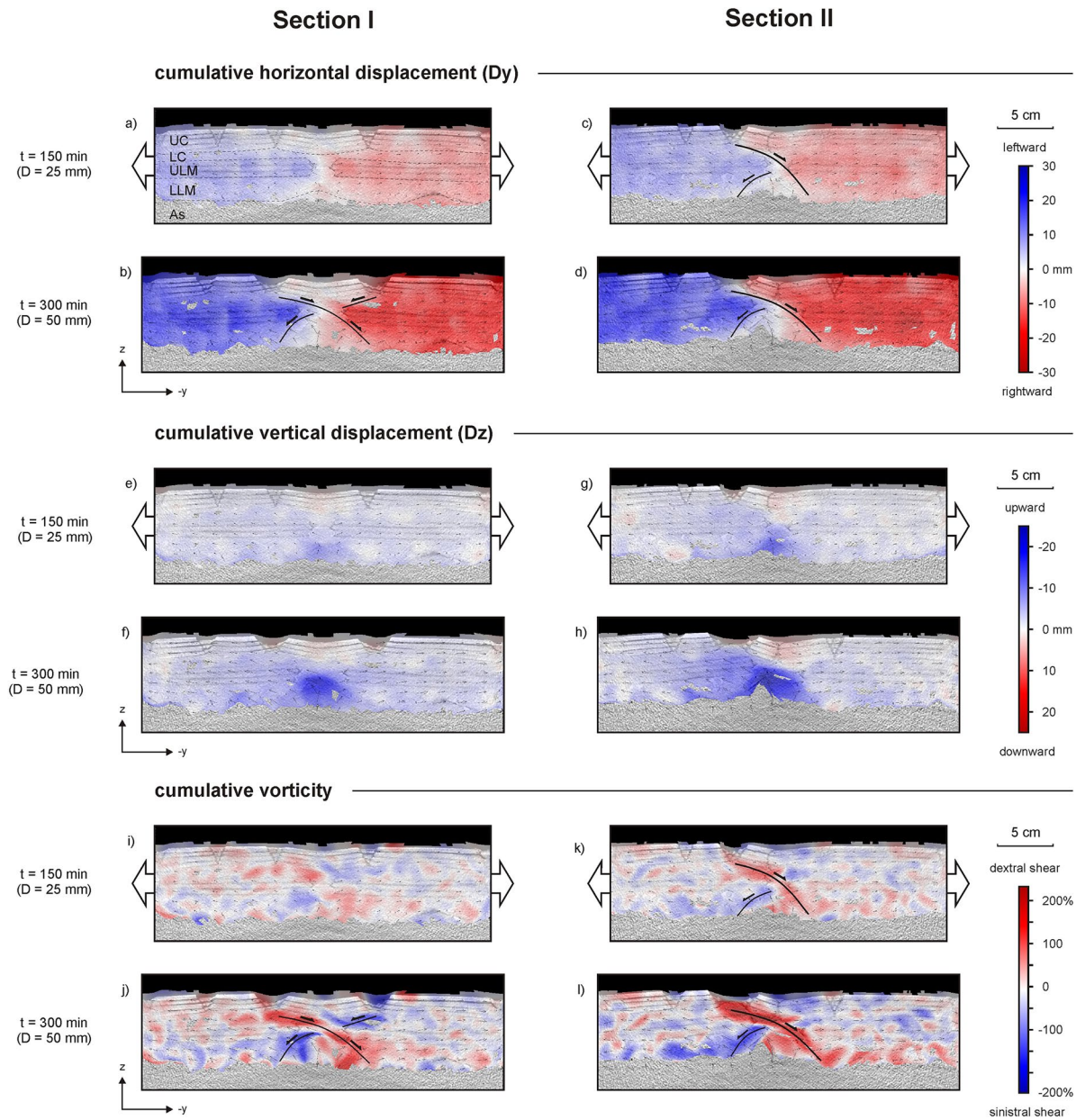

Figure 8. Results of digital image correlation (DIC) analysis on CT sections I and II from Model C. D: total divergence (for definition see Figure 2f). (a–d) Cumulative horizontal displacement (Dy) (e–h) Cumulative vertical displacement (Dz). (i–l) Cumulative vorticity. Section locations are indicated in Figure 5. UC: upper crust, LC: lower crust, ULM: upper lithospheric mantle, LLM: lower lithospheric mantle, As: asthenosphere.

double grabens (Figures 6f, 6g, 7a, 7c). The rifting also leads to substantial thinning of the modeled lower crust (and of the model lithosphere in general), which is accommodated by the strong rise of the lower lithospheric mantle layer and the modeled asthenosphere from $t = 120$ min on, putting the lower lithospheric mantle layer and upper crustal layer in near-direct contact towards the end of the model run (Figures 6g and 7c).

Section II is taken ca. 20 cm away to the right from Section I in Model C (Figures 5a–5e), and illustrates the development of an asymmetric double rift structure (Figures 6h–6n, 7b, 7d). Similar to Section I, initial deformation localizes in the upper lithospheric mantle layer (Figures 6b and 6i). However, an early asymmetric transfer of deformation to the modeled upper crust via a low-angle shear zone in the lower crustal layer causes the development of a graben on one side of the central model axis (Figure 6j). As rifting continues and the upper

lithospheric mantle is split apart, this graben continues evolving (Figures 6k–6n, 7c, 7d). In the meantime, a smaller secondary graben appears on the other side of the central model axis, whereas a curved fault develops in the center of the model (Figures 6m and 6n). Another minor graben develops away from the central model axis as well (Figure 6k–6n). Around this point in time (t = 120 min), the model asthenosphere and lower lithospheric mantle start to rise considerably, compensating the thinning of the lower mantle (and lithosphere in general) (Figure 6l–6n, 7b, 7d). As the model continues evolving, the initial graben remains dominant while the lithosphere continues thinning up to the point that the lower lithospheric mantle and upper crust are in contact (Figures 6n and 7d). It is also worth noting how much the upper lithospheric mantle to the left in Section II is strongly tilted upward when compared with the symmetric setting of Section I (Figures 7c and 7d).

3.3.3. DIC Analysis on CT Sections

In addition to visual inspection and interpretation of the CT imagery, we also apply DIC techniques to quantify model-internal deformation occurring in both Section I and II of Model C (Figure 8). Firstly, cumulative horizontal displacement data (Dy) reveals the development of differences in Dy values over time in both Section I and II (Figures 8a–8d). The symmetric rift structure in Section I is characterized by a stationary upper crustal block between two lithospheric domains that are diverging (Figures 8a and 8b). This arrangement is reminiscent of the stationary domain seen in DIC analysis of top view imagery in Models B and C (Figures 4f–4j and 5f–5j). By contrast, the asymmetric rift structure in Section II lacks such a stationary domain, as the diverging domains are in direct contact (Figures 8c and 8d). However, both sections have an additional low Dy domain in the lower part of the modeled lithosphere as well (Figures 8a–8d). Note that the boundaries between the different Dy domains in Sections I and II delineate the low-angle shear zones in the lower crust as identified on CT imagery (Figures 6g and 6n), as well as shear zones deeper in the lithosphere (Figures 8a–8d). In the case of the asymmetric rift structure in Section II, we observe a large-scale shear zone running through the whole lithosphere (Figures 8c and 8d).

In addition to horizontal displacement values, we also present vertical displacement values (Dz) and cumulative vorticity data obtained through DIC analysis of CT sections (Figures 8e–8l). The Dz data reveal that the overall model lithosphere does not undergo significant vertical displacement (Figures 8e–8h), with the exception of the central rift zone, where the model surface is subsiding, and the model asthenosphere is strongly rising (as also visible in the profiles in Figure 7). The cumulative vorticity data indicate changes in displacement patterns, highlighting shear zones in the model, as well as their sense of shear (Figures 8i–8l). Although they are not highly precise, the shear zones indicated by the cumulative vorticity results are in good agreement with those previously interpreted through the CT imagery and the Dy data (Figures 6, 8a–8d, 8i–8l).

3.4. Oblique Rifting Model D

We present the topographic and surface DIC analysis of CT-scanned 45° oblique rifting Model D in Figure 9. During the first 195 min of deformation at the standard divergence rate of 10 mm/hr, the model is being stretched and a depression formed along its central axis. At t = 180 min some faint deformation zones on both sides of this depression become visible on the DIC results (Figures 9a–9c and 9g–9i). However, no clear faulting is observed, which is in clear contrast to the situation in orthogonal rifting Models B and C over the same period (Figures 4a–4d, 4f–4i, 5a–5d, 5f–5i, 9a–9c and 9g–9i).

In order to force deformation in the model, we triple the divergence rate to 30 mm/hr in the second phase of the model run, from t = 195 min onward. As a result, faulting starts to localize along the deformation zones flanking the central depression (Figures 9d, 9e, 9j–9k). These faults are arranged in a left-stepping en echelon fashion, leading to the development of two zones of en echelon grabens along the central axis of the model, flanked by a number of additional graben structures that are mostly located in the top-right corner (Figure 9f). However, these additional grabens (as well as the boundary effects along the long ends of the model) only accommodate a minor part of the total deformation, as demonstrated by our DIC results (Figures 9j–9l)

CT imagery, presented in Figure 10, provides insights into the internal deformation of Model D. The images show how during the first phase of the model run, deformation localizes along the seed, leading to the upper lithospheric mantle layer splitting apart (Figures 10a–10e). Yet, apart from some boundary effects along the long sidewalls, no clear faulting occurs in the upper crustal layer, as only the central depression seen on topography data develops (Figures 9a–9c and 10a–10e). The situation totally changes during the second model phase as faster rifting leads to the localization of faulting in the upper crustal layer, and the development of a symmetric

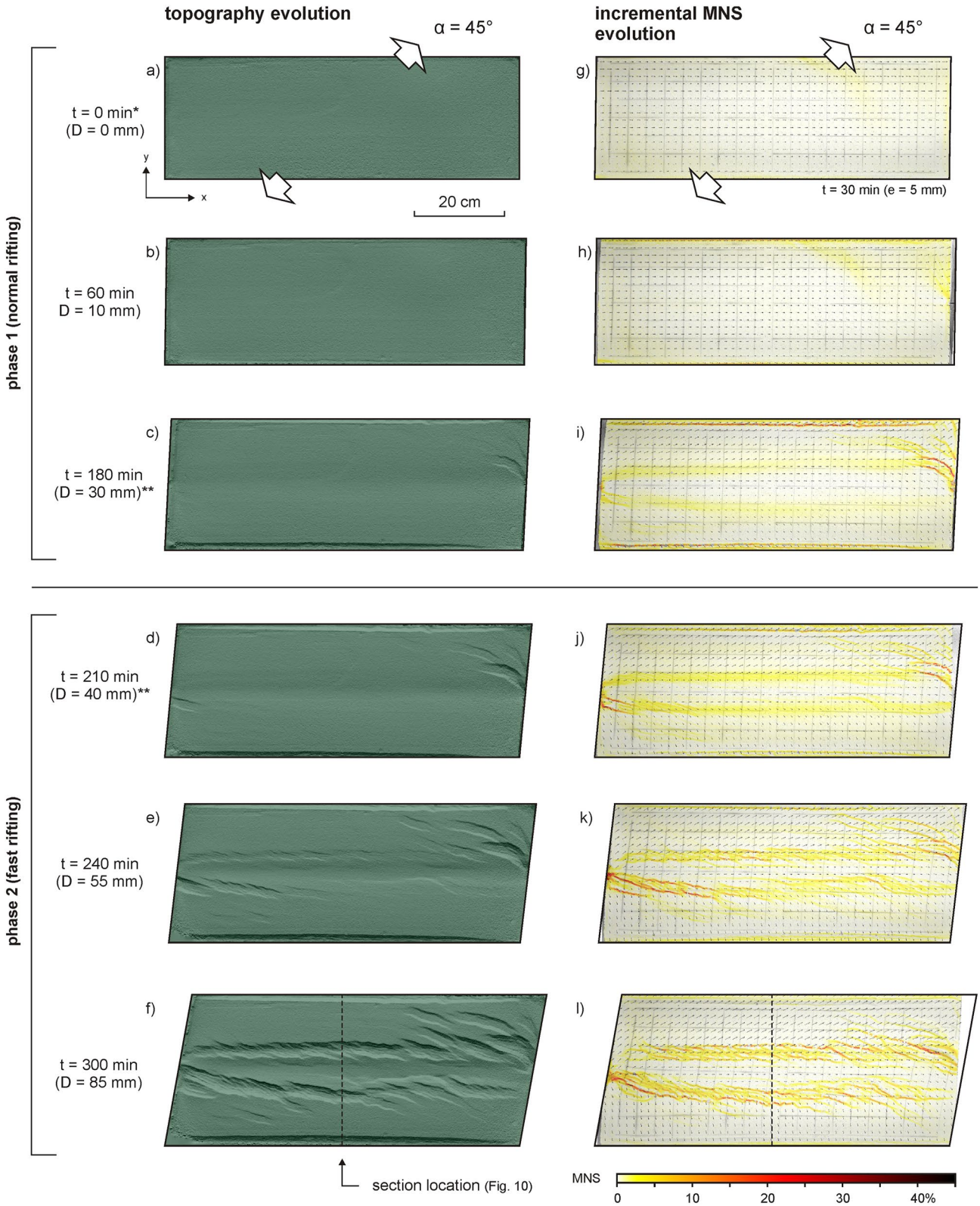

Figure 9. Topography and digital image correlation (DIC) analysis overview of 45° oblique rifting Model D. D: total divergence (for definition see Figure 2f). (a–f) Topography analysis, lighting from top. (g–l) DIC (incremental MNS [maximum normal strain]) analysis, representing the length of the longest axis of the strain ellipse in the horizontal plane, which is taken as a proxy for extensional deformation.

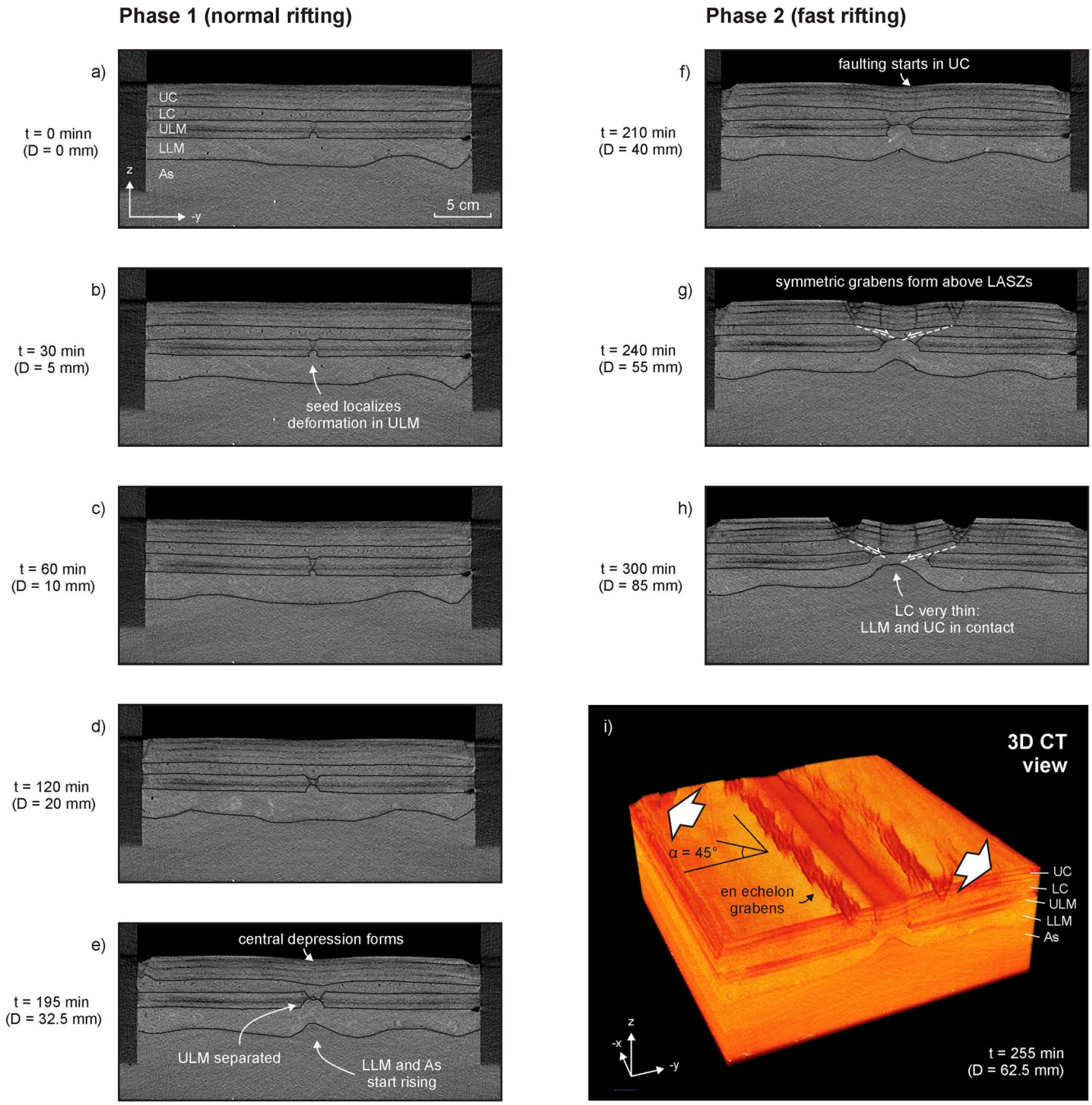

Figure 10. CT analysis 45° oblique rifting Model D. D: total divergence (for definition see Figure 2f). (a–e). Model evolution in section view during Phase 1 with the standard divergence velocity (10 mm/hr). (f–h) Model evolution in section view during fast rifting Phase 2 (30 mm/hr). (i) 3D CT image at $t = 255$ min (62.5 mm of divergence). LASZ: low-angle shear zone, UC: upper crust, LC: lower crust, ULM: upper lithospheric mantle, LLM: lower lithospheric mantle, As: asthenosphere.

double graben system (Figures 10f–10h). The en echelon nature of this double graben system, and its relation to the deformation deeper in the model lithosphere as well as the oblique divergence direction is revealed by 3D CT imagery (Figure 10i).

Due to the lateral displacement component in Model D, the same 2D DIC analysis on CT sections as shown for orthogonal extension Model C is not performed. However, we may assume that the 2D cumulative displacement and deformation patterns in Model D are broadly similar to those obtained for Section I from Model C, given the similarity in CT section view (Figures 6g and 10h).

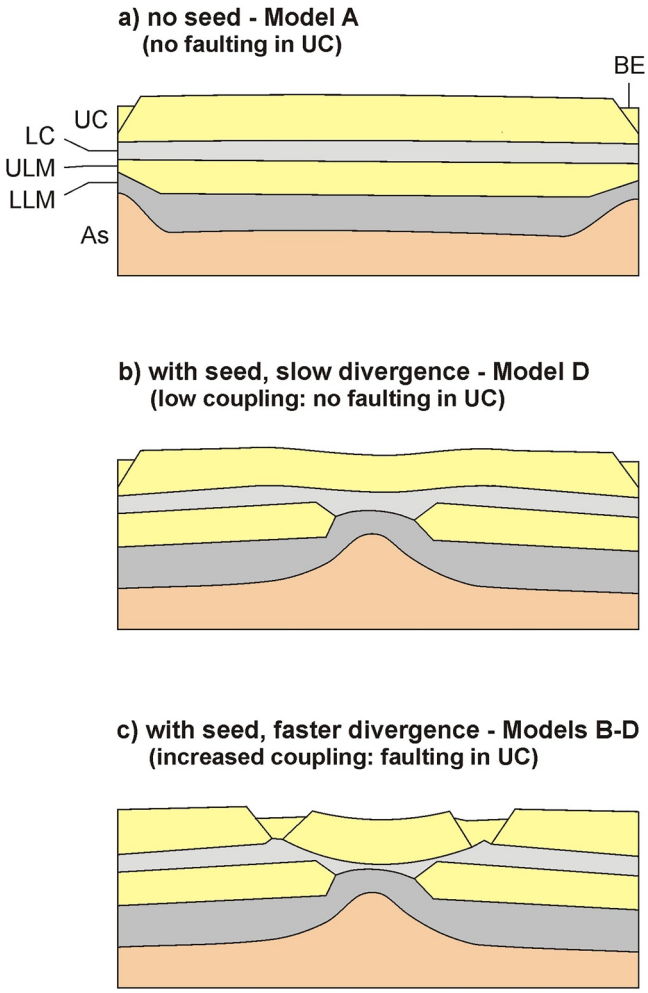

Figure 11. Schematic 2D overview of how seeds and the degree of coupling between the competent upper crust and upper lithospheric mantle layers (as a function of divergence velocity that affects the strength of the lower crustal layer) influences model development. BE: boundary effect, UC: upper crust, LC: lower crust, ULM: upper lithospheric mantle, LLM: lower lithospheric mantle, As: asthenosphere. (a) Situation in Model A, without seed and moderate divergence velocity, leading to the development of boundary effects only. (b) Situation during the first phase of Model D, with a seed but relatively slow divergence and a weaker lower crust, leading to low coupling so that the deformation in the upper lithospheric mantle does not induce faulting in the upper crustal layer. Instead, upper crustal faulting occurs in the shape of boundary effects along the longitudinal sides of the model. (c) Situation in Model B and C (with a seed and moderate divergence velocities) or in the second phase of Model D (with a seed and a high divergence velocity), leading to a stronger lower crust and sufficient coupling to transfer deformation from the upper lithospheric mantle into the upper crustal layer and to induce faulting there.

4. Discussion

Our model results obtained through a novel combination of external and internal monitoring and analysis techniques provide insights into three key topics: (a) the general localization of faulting, (b) symmetric and asymmetric rift systems, and (c) the development of rift systems in 3D during oblique extension. We summarize these results in text and figures (Figures 11–13), and compare them with results from previous modeling studies. Here it must be kept in mind that our models do not represent a systematic parameter study due to the variations in model parameters we apply. Still we believe the results are sufficiently robust for a productive discussion, especially when linked to observations from previously published modeling work. We subsequently describe the limitations of our modeling approach and potential future implementations for our understanding of natural systems, as well as of other tectonic settings.

4.1. Localization of Faulting: Effects of Seed and Coupling

The first key observations concern the general localization of deformation in our models, as summarized in section view in Figure 11. The absence of deformation in the form of faulting in the upper crustal layer along the central axis of Model A without a seed, highlights that such a seed is required to localize a rift structure in this model set-up (compare Model A with Models B-D, Figures 3–11a, 11c). The need for a seed or weakness to localize deformation in brittle-viscous set-ups has been shown by various previous analog and numerical modelers (e.g., Oliveira et al., 2022; Zwaan et al., 2019), and is linked to the decoupling effect of the weak viscous layer representing the lower crust. This decoupling isolates the competent brittle layers in the model lithosphere, and deformation will simply focus along the sidewalls, which form the weakest part of the model, whereas the brittle layers simulating the upper crust and upper lithospheric mantle remain stationary and undeformed. However, in other analog modeling studies of lithospheric-scale rifting, researchers induce deformation by using a narrower set-up with U-shaped sidewalls (e.g., Allemand & Brun, 1991; Autin et al., 2010; Brun & Beslier, 1996; Nestola et al., 2013, 2015). The edges of these U-shaped sidewalls act as velocity discontinuities (VDs), triggering deformation along the central model axis. But as pointed out by Zwaan et al. (2019), and even partiality visible at the short ends of our models as well (Figure 5), faulting then tends to initiate at these VDs before growing toward the center of the model.

Furthermore, our models show that divergence velocity affects the strength coupling between the competent (brittle) layers and plays an important role in the localization of faulting as well. Orthogonal rifting models B and C generate double graben structures due to a transfer of deformation from the seed in the upper lithospheric mantle through the lower crust into the upper crust via low-angle shear zones (Figure 6). However, such transfer of deformation does not occur in (the initial phase of oblique rifting of) Model D, where only a central depression forms, with some faulting along the sidewalls, whereas the upper lithospheric mantle layer splits apart due to the presence of the seed (Figures 10 and 11b). This difference is likely (partially) caused by the orthogonal divergence velocity component (Y1 + Y2, which determines the amount of new area created in the system) during the first phase of Model D being smaller than in Models B and C (Table 2). As a result of this lower initial orthogonal divergence velocity in Model D, the strength of the lower crustal layer, which has a strain-rate dependent rheology, seems to be reduced. Therefore, the upper lithospheric mantle and upper crustal layers are more decoupled and localized deformation cannot be transferred between

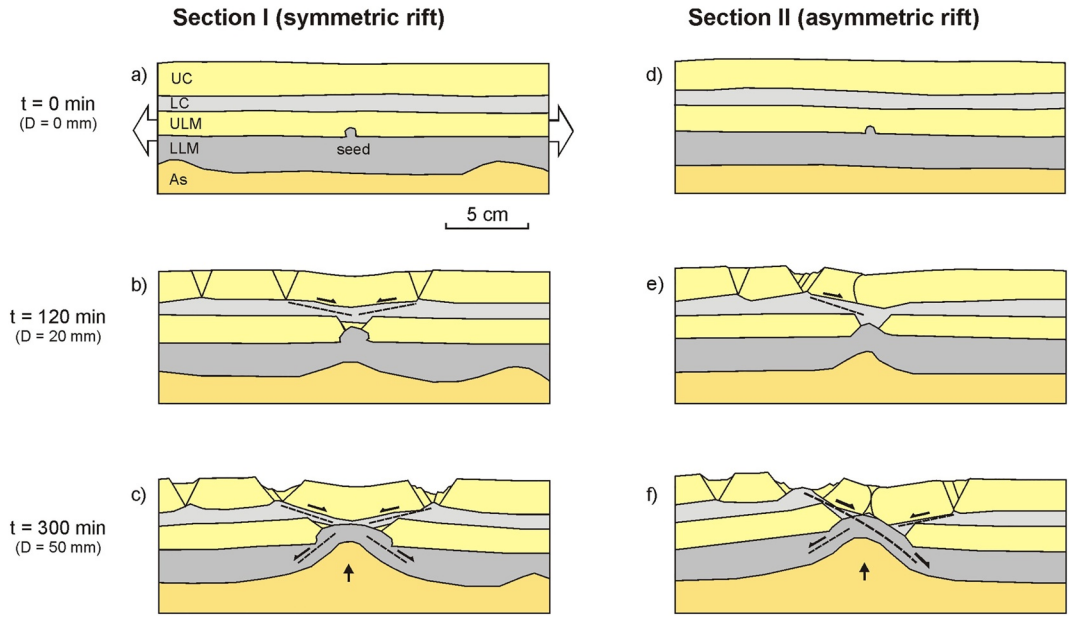

Figure 12. Schematic evolution of (a–c) symmetric versus (d–f) asymmetric rift systems (right), based on CT imagery from orthogonal rifting Model C (Figure 6). UC: upper crust, LC: lower crust, ULM: upper lithospheric mantle, LLM: lower lithospheric mantle, As: asthenosphere.

both these competent layers (e.g., Brun, 1999, 2002; Michon & Merle, 2000, 2003; Zwaan et al., 2019). Vice versa, faster rifting, as in Phase 2 of Model D, increases coupling, leading to the initiation of faulting in the upper crustal layer due to transfer of localized deformation from the seed upward, whereas faulting along the sidewalls is reduced (Figures 9, 10, and 11c). These findings are in accordance with previous modeling work showing that faster divergence allows (localized) deformation in the mantle to have more influence on upper crustal faulting, or to even overprint and suppress deformation otherwise occurring along weaknesses in the upper crust, leading to complex interactions and intricate rift structures (Zwaan et al., 2021; Zwaan, Chenin, et al., 2022).

4.2. Symmetric Versus Asymmetric Rift Development

The orthogonal rifting Models B and C, both with seeds, provide important insights in the development of symmetric and asymmetric rift structures, as summarized in section view in Figure 12.

Both Models B and C show the development of symmetric rift structures as a result of symmetric transfer of deformation from the seed in the competent lithospheric mantle into the upper crustal layer (Figures 4 and 5, Section I in Figures 6–8, 12). As described in the preceding paragraph, a degree of coupling related to a moderate divergence rate is needed for this deformation transfer, which occurs along two shear zones in the lower crustal layer. The development of such double shear zones and associated double graben structures has been observed in both lithospheric-scale analog models (e.g., Brun & Beslier, 1996; Michon & Merle, 2000, 2003; Nestola et al., 2015), as well as in crustal-scale brittle-viscous models, where instead of a seed the edge of a base plate (VD) represents a fault in the upper lithospheric mantle (e.g., Allemand et al., 1989; Michon & Merle, 2000, 2003; Zwaan et al., 2019, 2021; Zwaan, Chenin, et al., 2022). Moreover, they are also observed in numerical modeling studies (Chenin et al., 2018, 2020; Dyksterhuis et al., 2007; Oliveira et al., 2022). In the case of a symmetric rift structure, two of these shear zones form simultaneously on both sides of the seed, causing the development of two equally sized grabens in the upper crustal layer, with a relatively undeformed "H-block" (i.e., "hanging wall block," Lavier & Manatschal, 2006; Péron-Pinvidic & Manatschal, 2010) in between (Figures 12b and 12c).

By contrast, in some parts of Model C, the rift structure develops in an asymmetric fashion (Figure 5, Section II in Figures, 6–8, 12). In this asymmetric system we find the early development of a single shear zone in the lower crust, inducing a single graben in the upper crust early on (Figure 12e). In later stages, a second shear zone may develop, but the initial shear zone remains dominant and evolves into a large shear zone crossing the whole lithosphere, whereas the lower crust is exhumed at the bottom of the dominant graben (Figure 12f). It is not clear why this asymmetry occurs in (parts of) Model C, especially since the structures in the equivalent Model

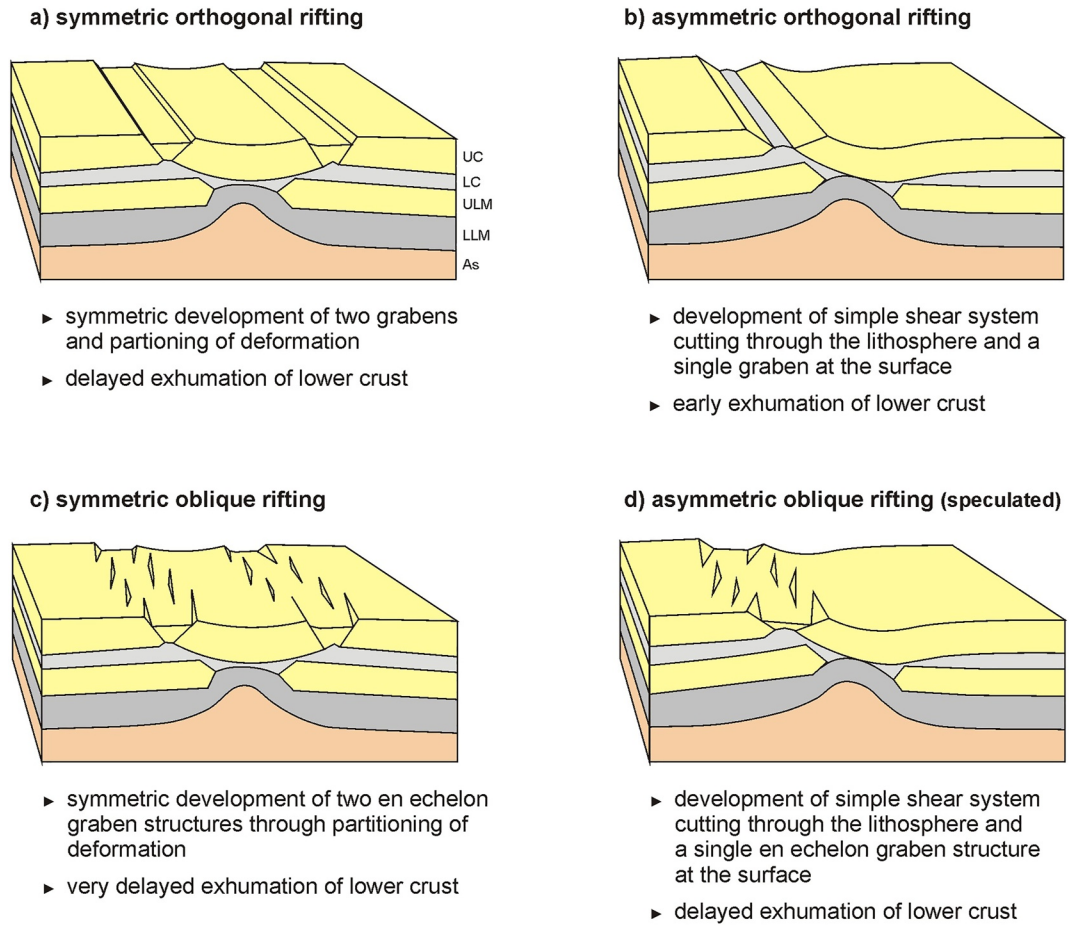

Figure 13. 3D sketches of final model results, depicting the difference between rift structures developing in (a) a symmetric orthogonal rift system (Models B, C), (b) an asymmetric orthogonal rift system (parts of Model C), (c) (fast) symmetric oblique rifting (Model D), and (d) the speculated result of a model with (fast) symmetric oblique rifting. UC: upper crust, LC: lower crust, ULM: upper lithospheric mantle, LLM: lower lithospheric mantle, As: asthenosphere.

B are fully symmetrical (compare Figures 4 and 5), but previous analog models show that the mode of rifting is influenced by the divergence rate (Brun & Beslier, 1996; Michon & Merle, 2003). We therefore speculate that the set-up we apply in our models is close to a tipping point, so that small differences in model preparation, which are known to affect analog modeling results (e.g., Schreurs et al., 2006, 2016), may locally shift the system from a symmetrical to an asymmetrical style, and vice versa. Furthermore, numerical modeling studies show that a variety of additional factors can affect the symmetry of a rift system (e.g., Brune et al., 2014; Huismans & Beaumont, 2002, 2003; Huismans et al., 2005; Nagel & Buck, 2004), but a detailed comparison of our analog models with these numerical results is beyond the scope of this paper.

However, even though we cannot pinpoint with certainty what causes the shift in rift style in this study, our new models allow us to examine and compare both symmetric and asymmetric rifting situations. In both cases we find a sharp rise of the asthenosphere, isostatically compensating the strong thinning of the lithosphere, which in the center chiefly consists of upper crustal and lower lithospheric mantle material as both the lower crust and upper lithospheric mantle are practically split in two (Figure 6g, 6n, 7, 12c, 12f). This rise of the asthenosphere is a universal observation in other lithospheric-scale analog and numerical models undergoing strongly localized thinning (e.g., Allemand et al., 1989; Brun & Beslier, 1996; Brune et al., 2014; Chenin et al., 2018, 2020; Nestola et al., 2013, 2015), and prevents the local "collapse" of the modeled lithosphere that may occur in advanced stages of rifting if no such isostatic compensation is included. Furthermore, there is no unrealistic regional subsidence of undeformed parts of the lithosphere due to stretching of the model and viscous thinning of lower crustal layer, previously observed in two-layer brittle-viscous models (e.g., Schmid et al., 2022a, 2022b; Zwaan et al., 2020).

4.3. Oblique Extension and 3D Rift Structures

Apart from purely 2D considerations detailed in the previous sections, our orthogonal and oblique rifting models also provide insights into 3D rift development (summarized in Figure 13). Orthogonal divergence Models B and C generate symmetric and asymmetric rift systems with through-going faults parallel to the long axis of the models (Figures 4, 5, 13a, 13b). By contrast, oblique divergence Model D, after developing only limited faulting in the upper crust during the initial rifting phase, forms two series of obliquely oriented basins during the second, faster divergence phase (Figures 9, 10i, 13c). These series of left-stepping en echelon basins follow in fact the trace of the double grabens in the orthogonal divergence situation (Figure 13a). This indicates that, after increasing the divergence velocity in the second phase of Model D, the lower crust with its strain rate-dependent rheology is sufficiently strengthened to allow for the development of shear zones in the lower crust that transfer deformation (coupling) from the seed in the upper lithospheric mantle into the upper crustal layer (Figure 13a). Note that one needs to be careful when comparing model D with models B and C, due to the application of the second phase of faster rifting in Model D. Still, Model D illustrates what structures may be expected in oblique rift settings.

Indeed, within this general framework, the en echelon faults themselves are typical of oblique rift systems, as normal faults form perpendicular to the (local) extension direction (which itself may deviate from the plate divergence direction in oblique divergence settings, Withjack & Jamison, 1986). Examples of en echelon faulting in oblique divergence settings are found in lithospheric-scale analog and numerical models (e.g., Agostini et al., 2009; Autin et al., 2010, 2013; Brune, 2014; Duclaux et al., 2020), as well as in crustal-scale experiments applying a brittle-viscous base plate set-up also reproduced the double graben style with en echelon faulting (e.g., McClay & White, 1995; Tron & Brun, 1991; Zwaan et al., 2021; Zwaan, Chenin et al., 2022). These findings indicate that some aspects of lithospheric-scale models (i.e., deformation in the crustal parts) can be well-represented by simpler crustal-scale models, which was previously suggested by Michon and Merle (2003) as well.

Finally, even though not observed in our study, there is a good possibility that, similar to their orthogonal divergence counterparts, oblique divergence models could develop asymmetric rift systems with a single zone of en echelon faulting (Figure 13d). As in the case of the orthogonal divergence models, an asymmetric rift under oblique divergence conditions would lead to earlier exhumation of the lower crust than in the symmetric equivalent as all deformation would be localized in one graben. However, this lower crustal exhumation would itself be delayed compared to the lower crustal exhumation in the orthogonal divergence models, due to the smaller orthogonal divergence component (Y1 + Y2) applied in our oblique divergence set-up (Figures 2f and 13, Table 2).

4.4. Model Limitations, and Opportunities for Improvement and New Studies

Our novel application of CT-scanning as well as subsequent DIC analysis on CT imagery is a significant step forward in the field of analog modeling of lithospheric-scale rifting. It provides us with unprecedented insights into the internal deformation evolution of such lithospheric-scale models (Figures 3, 6, 7, 8, and 10). Especially the quantification of deformation over time in these models by means of DIC analysis on CT imagery (Figure 8) allows for direct comparisons with numerical modeling studies. Additional steps could involve the expansion of our 2D DIC analysis into the third dimension (so-called digital volume correlation or DVC analysis applied on CT volumes, Adam et al., 2013; Poppe et al., 2019; Schmid et al., 2022a, 2022b; Zwaan, Schreurs, & Adam, 2018) to fully quantify the evolution of internal model deformation in 3D. However, the resolution (512 × 512 pixels) of standard medical CT scanners poses a limitation here. The imagery allows for excellent visual inspection and interpretation, but the resolution is relatively low for detailed DIC analysis. This limitation could however be mitigated to a degree by applying (industrial) CT scanners with higher resolution, by selecting a smaller scan window, or by applying thicker model layering. As a matter of fact, the 8-cm-thick lithosphere we apply is already much thicker than in most other analog modeling studies, and has been intentionally increased to improve the resolution of our results (compare the scans from Model A with those from Models B and C, Figures 3, 6 and 10). We estimate that a further doubling of this lithospheric thickness would be feasible.

The new set-up and general modeling approach itself has also proven itself to be successful. However, the procedure is somewhat challenging due to the limitation imposed by the requirements for CT-scanning: the materials need to be X-ray transparent, and the whole set-up needs to fit into a CT scanner (Figure 2b). As a result, the syrup basin is relatively small, so that adding the relatively thick lithosphere risks causing large displacement of syrup,

in contrast to other modeling set-ups that either have much larger basins or much thinner lithospheres. Our solution to freeze the syrup for stability during model preparation means that completing a single model takes a week, limiting the modeling output (see details in Zwaan & Schreurs, 2023a). This lower output is however more than offset by the CT-scanning results, and it would be possible to prepare multiple models in parallel to double or triple the modeling output. Furthermore, this new set-up allows for easy simulation of different degrees of oblique divergence, and as such the study of 3D tectonic processes in rift systems (Figures 2f, 9, 10, and 13).

A further consideration is the lithospheric layering and model materials. Various authors have applied different lithospheric layering (e.g., Allemand et al., 1989), and we have only explored a very small part of the potential parameter space. Rerunning models with these different types of lithospheric layering in the CT scanner would allow for new insights. Moreover, a limitation in most analog models of lithospheric-scale rifting has always been that most materials generally do not undergo thermal effects. This may not be much of an issue in models such as those presented in this paper, which mainly aim at the earlier stages of rifting when thermal effects are considered of minor importance (Zwaan et al., 2021; Zwaan, Chenin, et al., 2022). However, as the lithosphere starts necking, and the hot asthenosphere starts rising to the surface (Figures 6, 7, 8, 10, and 12), we should expect phase changes and variations in rheology to kick in. Therefore, the inclusion of model materials, of which the rheology is affected by temperature changes (e.g., Boutelier et al., 2003, 2012; Boutelier & Oncken, 2011; Chemenda et al., 2002; Krýza et al., 2019), in CT-scanned models of lithospheric-scale rifting would be a promising avenue for future studies. This could be combined with parallel numerical modeling efforts, which will allow for both benchmarking and verification of both modeling methods (e.g., Brune et al., 2017; Panien et al., 2006; Zwaan et al., 2016), and for the addition of other parameters that are challenging to include in lithospheric-scale analog models (e.g., surface processes). In this context, it is also important to stress that the current method is only suitable for the modeling of magma-poor rift settings, since magmatism can strongly affect rift evolution (e.g., Buck, 2004, 2006).

Finally, we see great opportunities beyond the field of rifting, as our new method could also be applied for the simulation and detailed analysis of (oblique) collisional tectonics (e.g., Calignano et al., 2015, 2017; Luth et al., 2010; Sokoutis & Willingshofer, 2011; Willingshofer et al., 2013; Willingshofer & Sokoutis, 2009) and lithospheric-scale basin inversion (Boutelier et al., 2003; Cerca et al., 2005; Gartrell et al., 2005).

5. Conclusion and Future Outlook

In this paper we present a novel method for the modeling of (magma-poor) lithospheric-scale rifting processes, which can be uniquely monitored in a CT scanner. We show how the application of CT-scanning and DIC analysis on CT imagery provides unparalleled details regarding the (internal) evolution of such lithospheric-scale models, and our first set of models provides the following first-order insights:

- The degree of coupling between the competent layers in the lithosphere in the presence of a weak lower crust has an important influence on the development of the modeled rift system. Low coupling due to slow rifting isolates the upper crust from the upper lithospheric mantle layer below, preventing an efficient transfer of deformation between both layers. By contrast, fast rifting increases coupling and allows deformation in the mantle to efficiently induce deformation in the upper crust.
- When sufficient coupling occurs and deformation is transferred from the mantle into the upper crust, we observe either the development of a symmetric or asymmetric (double) rift system in our models. Although the reason why the system may develop one or the other style is not fully clear, we obtain detailed insight in the evolution of either style.
- Oblique divergence leads to en echelon graben arrangements, and a delayed exhumation of lower crustal material. We speculate that these structures may occur in both symmetric or asymmetric (double) rift systems.

These initial models provide an incentive to further simulate rifting processes on lithospheric scales, and to apply advanced techniques to extract as much information as possible out of these. There is indeed a broad range of opportunities for improvements to our new modeling method, for example, involving the testing of different lithospheric layering and the inclusion of new materials with temperature-sensitive rheology, for new studies within and beyond the field of rift tectonics.

Appendix A: Model Scaling

Applying analog modeling scaling laws (e.g., Hubbert, 1937; Ramberg, 1981; Weijermars & Schmeling, 1986) demonstrates the suitability of our models for simulating continental rifting processes. The parameters for our scaling calculations are provided in Table A1.

The standard length scaling ratio (h^*) in our models was $6.7 \cdot 10^{-7}$ (ratio convention: model/nature), so that 1 cm correspond to 15 km in nature, and the whole 6.5 cm thick model layering represents a ca. 100 km thick lithosphere. The density ratio (ρ^*) and gravity ratio (g^*) were ca. 0.45, and 1 in our models, respectively. Using these data we obtained the stress ratio (σ^*) via the following equation (Hubbert, 1937; Ramberg, 1981): $\sigma^* = \rho^* \cdot h^* \cdot g^*$. Here ρ^*, h^* and g^* represent the density, length and gravity ratios respectively, and the equation yields a σ^* of ca. $3 \cdot 10^{-7}$.

Table A1
Scaling Details (for Standard Model Parameters)

		Model	Nature
General parameters	Gravitational acceleration (g)	9.81 m/s^2	9.81 m/s^2
	Divergence velocity (v)[a]	$2.7 \cdot 10^{-6}$ m/s	$2.5 \cdot 10^{-9}$ m/s
Upper crust (UC)	Material	Feldspar sand	Upper crustal rocks
	Peak internal friction angle (φ)	35°	30-38°
	Thickness (h)	$2 \cdot 10^{-2}$ m	$3 \cdot 10^{4}$ m
	Density (ρ)	1,300 kg/m^3	2,800 kg/m^3
	Cohesion (C)	51 Pa	$1.6 \cdot 10^{8}$ Pa
Lower crust (LC)	Material	Viscous mixture 1	Lower crustal rocks
	Thickness (h)	$1 \cdot 10^{-2}$ m	$1.5 \cdot 10^{4}$ m
	Density (ρ)	1,300 kg/m^3	2,900 kg/m^3
	Viscosity (η)	$6 \cdot 10^{4}$ Pa·s	$1 \cdot 10^{22}$ Pa·s
Upper lithospheric mantle (ULM)	Material	Feldspar sand	Peridotite
	Peak internal friction angle (φ)	35°	30-38°
	Thickness (h)	$1.5 \cdot 10^{-2}$ m	$2.25 \cdot 10^{4}$ m
	Density (ρ)	1,300 kg/m^3	3,300 kg/m^3
	Cohesion (C)	51 Pa	$2 \cdot 10^{8}$ Pa
Lower lithospheric mantle (LLM)	Material	Viscous mixture 2	Peridotite
	Thickness (h)	$2 \cdot 10^{-2}$ m	$3 \cdot 10^{4}$ m
	Density (ρ)	1,400 kg/m^3	3,300 kg/m^3
	Viscosity (η)	$8 \cdot 10^{4}$ Pa·s	$1.2 \cdot 10^{22}$ Pa·s
Asthenosphere	Material	Glucose syrup	Peridotite
	Thickness (h)	-	-
	Density (ρ)	1,450 kg/m^3	3,300 kg/m^3
	Viscosity (η)	65 Pa·s	$9 \cdot 10^{18}$ Pa·s
Dynamic scaling values	Brittle stress ratio (R_s)		
	UC	5.2	5.2
	ULM	3.75	3.5
	Ramberg number (R_m)		
	LC	7.2	7.1
	LLM	6.2	6.1
	As	$7.9 \cdot 10^{3}$	$7.9 \cdot 10^{3}$

[a]Model B with standard extension rate of 10 mm/hr, translating to 2.6–3.1 mm/yr in nature for the scaling values presented in this table.

For brittle materials, scaling is relatively straightforward due to their strain-rate independent rheology. Most important is the internal friction angle of the feldspar sand we used, which is very similar that of upper crustal rocks (e.g., Byerlee, 1978; Table A1). The dynamic similarity in the brittle layers can be validated by calculating the R_s ratio (Bonini et al., 2001; Mulugeta, 1988; Ramberg, 1981): R_s = gravitational stress/cohesive strength = $(\rho \cdot g \cdot h)/C$. Here ρ is the density, g the gravitational acceleration, h the height and C cohesion of the brittle materials. Our calculations yield R_s values for the upper crust and upper lithospheric mantle that very similar between model and nature (Table A1), confirming the adequate dynamic scaling of the brittle behavior of the materials in our models.

Scaling of viscous materials is more complex due to their strain-rate dependent rheology. In the case of viscous materials, the stress ratio (σ^*) and viscosity ratio (η^*) produce the strain rate ratio ($\dot{\varepsilon}^*$) according to the ensuing formula: $\dot{\varepsilon}^* = \sigma^*/\eta^*$ (Weijermars & Schmeling, 1986), which is in the order of $1 \cdot 10^{10}$. Subsequently, we can obtain the velocity ratio v^* and time ratios t^* through the following equations: $\dot{\varepsilon}^* = v^*/h^* = 1/t^*$. As a result, our standard divergence velocity of 10 mm/hr translates to 2.6–3.1 mm/yr in nature, which is similar to divergence rates observed in nature (e.g., Saria et al., 2014).

To test dynamic similarity of the viscous layers, we apply the Ramberg number R_m (Weijermars & Schmeling, 1986): $R_m = (\rho \cdot g \cdot h^2)/(\eta \cdot v)$. The R_m values obtained for the different viscous layers in our models are very similar to the R_m values for their natural counterparts (Table A1). Together with the R_s values the Ramberg numbers indicate that scaling requirements are reasonably fulfilled for our standard model runs.

In the case of Model A, with half the layer thickness, the scaling is still adequate, but the divergence rate of 10 mm/hr, translates to 11 mm/yr. In the case of the enhanced divergence velocity in Model D, scaling remains according to the standard model parameters in Table A1, except that the 30 mm/hr divergence velocity during the second model phase translates to 9.6 mm/yr. These divergence velocities of 11 and 9.6 mm/yr are somewhat at the high end in nature. However, in the case of Model A did not significantly affect model evolution due to the decoupling between the model layers and the lack of a seed, whereas the increased coupling is needed in Model D, in order to force localization. Note that in the case of Model D, a slower divergence (e.g., 15 mm/h, translating to 4.8 mm/yr) may also have sufficed, but we chose to somewhat force the system in order to obtain a result.

Data Availability Statement

Supplementary material is available in the form of publicly accessible data publications, stored at the servers of GFZ Data Services. New details on the material properties of the glucose syrup and feldspar sand used in these models can be found in Schmid et al., 2022c (https://doi.org/10.5880/fidgeo.2022.030), and Zwaan, Schreurs, et al., 2022 (https://doi.org/10.5880/fidgeo.2022.008), respectively. Videos depicting the evolution of the model results and analyses (both in surface view and in [CT] section view) are provided in Zwaan & Schreurs, 2023a (https://doi.org/10.5880/fidgeo.2023.006). Detailed background on the modeling method itself can be found in Zwaan & Schreurs, 2023b (https://doi.org/10.5880/fidgeo.2023.005).

Acknowledgments
The initial inspiration for developing this new modeling approach was sparked by discussions with Yago Nestola, who was working at the University of Parma at the time. We would furthermore like to thank the engineers from IPEK Rapperswil (Dario Niggli, Peter Eichenberger, Rudolf Kamber, and Theodor Wüst) for working out our initial design and for constructing the components for the new model set-up. We are grateful to Nicole Schwendener from the Institute of Forensic Medicine (University of Bern) for helping us scan our models. Discussions with Nicolas Molnar (RWTH Aachen University) helped to improve the model design. Thanks also to Timothy Schmid from the Tectonic Modeling group at the Institute of Geological Sciences (University of Bern) for helping with the DIC analysis and the syrup testing, and to Kirsten Elger and Florian Ott from GFZ Potsdam for helping us prepare the GFZ data publications containing the supplementary data of this paper (Schmid et al., 2022c; Zwaan & Schreurs, 2023a, 2023b, and Zwaan, Schreurs, et al., 2022). We are grateful to Donna Shillington and an anonymous reviewer for providing useful feedback that helped us to improve the paper, and we thank editor Laurent Jolivet for providing additional input and guiding the overall review process. This project was funded by the Swiss National Science Foundation, Grant 200021-178731 "4D Analog modeling of oblique rifts and obliquely rifted margins" (https://data.snf.ch/grants/grant/178731). FZ was furthermore supported by a GFZ Discovery Fund fellowship. Open Access funding enabled and organized by Projekt DEAL.

References

Adam, J., Klinkmüller, M., Schreurs, G., & Wieneke, B. (2013). Quantitative 3D strain analysis in analogue experiments simulating tectonic deformation: Integration of X-ray computed tomography and digital volume correlation techniques. *Journal of Structural Geology*, *55*, 127–149. https://doi.org/10.1016/j.jsg.2013.07.011

Adam, J., Urai, J. L., Wieneke, B., Oncken, O., Pfeiffer, K., Kukowski, N., et al. (2005). Shear localisation and strain distribution during tectonic faulting—new insights from granular-flow experiments and high-resolution optical image correlation technique. *Journal of Structural Geology*, *27*(2), 283–301. https://doi.org/10.1016/j.jsg.2004.08.008

Agostini, A., Corti, G., Zeoli, A., & Mulugeta, G. (2009). Evolution, pattern, and partitioning of deformation during oblique continental rifting: Inferences from lithospheric-scale centrifuge models. *Geochemistry, Geophysics, Geosystems*, *10*, Q11015. https://doi.org/10.1029/2009GC002676

Allemand, P., & Brun, J.-P. (1991). Width of continental rifts and rheological layering of the lithosphere. *Tectonophysics*, *188*(1–2), 63–69. https://doi.org/10.1016/0040-1951(91)90314-I

Allemand, P., Brun, J.-P., Davy, P., & Van den Driessche, J. (1989). Symétrie et asymétrie des rifts et mécanismes d'amincissement de la lithosphere. *Bulletin de la Société Géologique de France*, *V*(3), 423–436. https://doi.org/10.2113/gssgfbull.V.3.445

Alonso-Henar, J., Schreurs, G., Martinez-Díaz, J. J., Álvarez-Gómez, J. A., & Villamor, P. (2015). Neotectonic development of the El Salvador Fault Zone and implications for deformation in the Central America Volcanic Arc: Insights from 4-D analog modeling experiments. *Tectonics*, *34*(1), 133–151. https://doi.org/10.1002/2014TC003723

Autin, J., Bellahsen, N., Husson, L., Beslier, M.-O., Leroy, S., & d'Acremont, E. (2010). Analog models of oblique rifting in a cold lithosphere. *Tectonics*, *29*(6), TC6016. https://doi.org/10.1029/2010TC002671

Autin, J., Bellahsen, N., Leroy, S., Husson, L., Beslier, M.-O., & d'Acremont, E. (2013). The role of structural inheritance in oblique rifting: Insights from analogue models and application to the Gulf of Aden. *Tectonophysics*, *607*, 51–64. https://doi.org/10.1016/j.tecto.2013.05.041

Bahroudi, A., Koyi, H. A., & Talbot, C. J. (2003). Effect of ductile and frictional décollements on style of extension. *Journal of Structural Geology*, *25*(9), 1401–1423. https://doi.org/10.1016/S0191-8141(02)00201-8

Benes, V., & Davy, P. (1996). Modes of continental lithospheric extension: Experimental verification of strain localization processes. *Tectonophysics*, *254*(1–2), 69–87. https://doi.org/10.1016/0040-1951(95)00076-3

Benes, V., & Scott, S. D. (1996). Oblique rifting in the Havre trough and its propagation into the continental margin of New Zealand: Comparison with analogue experiments. *Marine Geophysical Researches*, *18*(2–4), 189–201. https://doi.org/10.1007/BF00286077

Beniest, A., Willingshofer, E., Sokoutis, D., & Sassi, W. (2018). Extending continental lithosphere with lateral strength variations: Effects on deformation localization and margin geometries. *Frontiers in Earth Science*, *6*, 148. https://doi.org/10.3389/feart.2018.00148

Beslier, M.-O. (1991). *Formation des marges passives et remontée du manteau: Modélisation expérimentale et exemple de la marge de la Galice. Memoires et documents du Centre Armoricain d'etude structurale des socle, (Doctoral Dissertation)*. University Rennes 1. Retrieved from HAL https://tel.archives-ouvertes.fr/tel-00594598

Biggs, J., Ayele, A., Fischer, T. P., Fontijn, K., Hutchison, W., Kazimoto, E., et al. (2021). Volcanic activity and hazard in the East African Rift Zone. *Nature Communications*, *12*(1), 6881. https://doi.org/10.1038/s41467-021-27166-y

Bonechi, N., Fiaschi, D., Manfrida, L., Talluri, L., & Zuffi, C. (2021). Exploitation assessment of geothermal energy from African great rift valley. *E3S Web of Conferences*, *312*, 08008. https://doi.org/10.1051/e3sconf/202131208008

Bonini, M., Sokoutis, D., Mulugeta, G., Boccaletti, M., Corti, G., Innocenti, F., et al. (2001). Dynamics of magma emplacement in centrifuge models of continental extension with implications for flank volcanism. *Tectonics*, *20*(6), 1053–1065. https://doi.org/10.1029/2001TC900017

Boutelier, D., Chemenda, A., & Burg, J.-P. (2003). Subduction versus accretion of intra-oceanic volcanic arcs: Insight from thermo-mechanical analogue experiments. *Earth and Planetary Science Letters*, *212*(1–2), 31–45. https://doi.org/10.1016/S0012-821X(03)00239-5

Boutelier, D., & Oncken, O. (2011). 3-D thermo-mechanical laboratory modeling of plate-tectonics: Modeling scheme, technique and first experiments. *Solid Earth*, *2*(1), 35–51. https://doi.org/10.5194/se-2-35-2011

Boutelier, D., Oncken, O., & Cruden, A. (2012). Fore-arc deformation at the transition between collision and subduction: Insights from 3-D thermomechanical laboratory experiments. *Tectonics*, *31*, TC2015. https://doi.org/10.1029/2011TC003060

Boutelier, D., Schrank, C., & Regenauer-Lieb, K. (2019). 2-D finite displacements and strain from particle imaging velocimetry (PIV) analysis of tectonic analogue models with TecPIV. *Solid Earth*, *10*(4), 1123–1139. https://doi.org/10.5194/se-10-1123-2019

Brun, J.-P. (1999). Narrow rifts versus wide rifts: Inferences for the mechanics of rifting from laboratory experiments. *Philosophical Transactions of the Royal Society of London*, *357*(1753), 695–712. https://doi.org/10.1098/rsta.1999.0349

Brun, J.-P. (2002). Deformation of the continental lithosphere: Insights from brittle-ductile models. *Geological Society, London, Special Publications*, *200*(1), 355–370. https://doi.org/10.1144/GSL.SP.2001.200.01.20

Brun, J.-P., & Beslier, M.-O. (1996). Mantle exhumation at passive margins. *Earth and Planetary Science Letters*, *142*(1–2), 161–173. https://doi.org/10.1016/0012-821X(96)00080-5

Brun, J. P., Sokoutis, D., Tirel, C., Gueydan, F., Van Den Driessche, J., & Beslier, M.-O. (2018). Crustal versus mantle core complexes. *Tectonophysics*, *746*, 22–45. https://doi.org/10.1016/j.tecto.2017.09.017

Brune, S. (2014). Evolution of stress and fault patterns in oblique rift systems: 3-D numerical lithospheric-scale experiments from rift to breakup. *Geochemistry, Geophysics, Geosystems*, *15*(8), 392–3415. https://doi.org/10.1002/2014GC005446

Brune, S. (2016). Rifts and rifted margins: A review of geodynamic processes and natural hazards. In J. C. Duarte & W. P. Schellart (Eds.), *Plate boundaries and natural hazards* (pp. 13–37). https://doi.org/10.1002/9781119054146.ch2

Brune, S., Corti, G., & Ranalli, G. (2017). Controls of inherited lithospheric het-erogeneity on rift linkage: Numerical and analog models of interaction between the Kenyan and Ethiopian rifts across the Turkana depression. *Tectonics*, *36*(9), 1767–1786. https://doi.org/10.1002/2017TC004739

Brune, S., Heine, C., Pérez-Gussinyé, M., & Sobolev, S. V. (2014). Rift migration explains continental margin asymmetry and crustal hyper-extension. *Nature Communications*, *5*(1), 4014. https://doi.org/10.1038/ncomms5014

Buck, R. W. (2004). Consequences of asthenospheric variability on continental rifting. In G. Karner, B. Taylor, N. Driscoll, & D. Kohlstedt (Eds.), *Rheology and deformation of the lithosphere at continental margins* (pp. 1–29). https://doi.org/10.7312/karn12738-002

Buck, R. W. (2006). The role of magma in the development of the Afro-Arabian Rift System. *Geological Society, London, Special Publications*, *259*(1), 43–54. https://doi.org/10.1144/GSL.SP.2006.259.01.05

Burnside, N., Montcoudiol, N., Becker, K., & Lewi, E. (2020). Geothermal energy resources in Ethiopia: Status review and insights from hydrochemistry of surface and groundwaters. *Wiley Interdisciplinary Reviews: Water*, *8*(6), e1554. https://doi.org/10.1002/wat2.1554

Byerlee, J. (1978). Friction of rocks. *Pure and Applied Geosphysics*, *116*(4–5), 615–626. https://doi.org/10.1007/BF00876528

Calignano, E., Sokoutis, D., Willingshofer, E., Gueydan, F., & Cloetingh, S. (2015). Asymmetric vs. symmetric deep lithospheric architecture of intra-plate continental orogens. *Earth and Planetary Science Letters*, *424*, 38–50. https://doi.org/10.1016/j.epsl.2015.05.022

Calignano, E., Sokoutis, D., Willingshofer, E., Brun, J.-P., Gueydan, F., & Cloetingh, S. (2017). Oblique contractional reactivation of inherited heterogeneities: Cause for arcuate orogens. *Tectonics*, *36*(3), 542–558. https://doi.org/10.1002/2016TC004424

Capelletti, A., Tsikalas, F., Nestola, Y., Cavozzi, C., Argnani, A., Meda, M., & Salvi, F. (2013). Impact of lithospheric heterogeneities on continental rifting evolution: Constraints from analogue modelling on South Atlantic margins. *Tectonophysics*, *608*, 30–50. https://doi.org/10.1016/j.tecto.2013.09.026

Catuneanu, O., Abreu, V., Bhattacharya, J. P., Blum, M. D., Dalrymple, R. W., Eriksson, P. G., et al. (2009). Towards the standardization of sequence stratigraphy. *Earth-Science Reviews*, *92*(1–2), 1–33. https://doi.org/10.1016/j.earscirev.2008.10.003

Catuneanu, O., & Zecchin, M. (2013). High-resolution sequence stratigraphy of clastic shelves II: Controls on sequence development. *Marine and Petroleum Geology*, *39*(1), 26–38. https://doi.org/10.1016/j.marpetgeo.2012.08.010

Cerca, M., Ferrari, L., Corti, G., Bonini, M., & Manetti, P. (2005). Analogue model of inversion tectonics explaining the structural diversity of Late Cretaceous shortening in southwestern Mexico. *Lithosphere*, *2*(3), 172–187. https://doi.org/10.1130/L48.1

Chemenda, A., Déverchère, J., & Calais, E. (2002). Three-dimensional laboratory modelling of rifting: Application to the Baikal rift, Russia. *Tectonophysics*, *356*(4), 253–273. https://doi.org/10.1016/S0040-1951(02)00389-X

Chenin, P., Schmalholz, S. M., Manatschal, G., & Duretz, T. (2020). Impact of crust–mantle mechanical coupling on the topographic and thermal evolutions during the necking phase of 'magma-poor' and 'sediment-starved' rift systems: A numerical modeling study. *Tectonophysiscs*, *786*, 228472. https://doi.org/10.1016/j.tecto.2020.228472

Chenin, P., Schmalholz, S. M., Manatschal, G., & Karner, G. D. (2018). Necking of the lithosphere: A reappraisal of basic concepts with thermo-mechanical numerical modeling. *Journal of Geophysical Research: Solid Earth*, *123*, 5279–5299. https://doi.org/10.1029/2017JB014155

Colletta, B., Letouzey, J., Pinedo, R., Ballard, J. F., & Balé, P. (1991). Computerized X-ray tomography analysis of sandbox models: Examples of thin-skinned thrust systems. *Geology*, *19*(11), 1063–1067. https://doi.org/10.1130/0091-7613(1991)019<1063:CXRTAO>2.3.CO;2

Corti, G. (2008). Control of rift obliquity on the evolution and segmentation of the main Ethiopian rift. *Nature Geoscienc*e, 1(4), 258–262. https://doi.org/10.1038/ngeo160

Corti, G. (2012). Evolution and characteristics of continental rifting: Analog modeling-inspired view and comparison with examples from the East African Rift System. *Tectonophysics*, *522–523*, 1–33. https://doi.org/10.1016/j.tecto.2011.06.010

Corti, G., Bonini, M., Conticelli, S., Innocenti, F., Manetti, P., & Sokoutis, D. (2003). Analogue modelling of continental extension: A review focused on the relations between the patterns of deformation and the presence of magma. *Earth-Science Reviews*, *63*(3–4), 169–247. https://doi.org/10.1016/S0012-8252(03)00035-7

Corti, G., Ranalli, G., Agostini, A., & Sokoutis, D. (2013). Inward migration of faulting during continental rifting: Effects of pre-existing lithospheric structure and extension rate. *Tectonophysics*, *594*, 137–148. https://doi.org/10.1016/j.tecto.2013.03.028

Duclaux, G., Huismans, R. S., & May, D. A. (2020). Rotation, narrowing, and preferential reactivation of brittle structures during oblique rifting. *Earth and Planetary Science Letters*, *531*, 115952. https://doi.org/10.1016/j.epsl.2019.115952

Dyksterhuis, S., Rey, P., Müller, R. D., & Moresi, L. (2007). Effects of initial weakness on rift architecture. *Geological Society, London, Special Publication*, *282*(1), 443–455. https://doi.org/10.1144/SP282.18

Fedorik, J., Zwaan, F., Schreurs, G., Toscani, G., Bonini, L., & Seno, S. (2019). The interaction between strike-slip dominated fault zones and thrust belt structures: Insights from 4D analogue models. *Journal of Structural Geology*, *122*, 89–105. https://doi.org/10.1016/j.jsg.2019.02.010

Freymark, J., Sippel, J., Scheck-Wenderoth, M., Bär, K., Stiller, M., Fritsche, J.-H., & Kracht, M. (2017). The deep thermal field of the Upper Rhine Graben. *Tectonophysics*, *694*, 114–129. https://doi.org/10.1016/j.tecto.2016.11.013

Gartrell, A., Hudson, C., & Evans, B. (2005). The influence of basement faults during extension and oblique inversion of the Makassar Straits rift system: Insights from analog models. *American Association of Petroleum Geologists Bulletin*, *89*(4), 495–506. https://doi.org/10.1306/12010404018

Gouin, P. (1979). *Earthquake history of Ethiopia and the Horn of Africa*. International Development Research Centre, Canada.

Haq, B. U., Hardenbol, J., & Vail, P. R. (1987). Chronology of fluctuating sea levels since the triassic. *Science*, *235*(4793), 1156–1167. https://doi.org/10.1126/science.235.4793.1156

Holland, M., Van Gent, H., Bazalgette, L., Yassir, N., Hoogerduijn Strating, E. H., & Urai, J. L. (2011). Evolution of dilatant fracture networks in a normal fault — Evidence from 4D model experiments. *Earth and Planetary Science Letters*, *304*(3–4), 399–406. https://doi.org/10.1016/j.epsl.2011.02.017

Hubbert, M. K. (1937). Theory of scale models as applied to the study of geologic structures. *The Geological Society of America Bulletin*, *48*(10), 1459–1520. https://doi.org/10.1130/GSAB-48-1459

Huismans, R. S., & Beaumont, C. (2002). Asymmetric lithospheric extension: The role of frictional plastic strain softening inferred from numerical experiments. *Geology*, *30*(3), 211–214. https://doi.org/10.1130/0091-7613(2002)030<0211:ALETRO>2.0.CO;2

Huismans, R. S., & Beaumont, C. (2003). Symmetric and asymmetric lithospheric extension: Relative effects of frictional-plastic and viscous strain softening. *Journal of Geophysical Research*, *108*(B10), 2496. https://doi.org/10.1029/2002JB002026

Huismans, R. S., Buiter, S. J. H., & Beaumont, C. (2005). Effect of plastic-viscous layering and strain softening on mode selection during lithospheric extension. *Journal of Geophysical Research*, *110*, B02406. https://doi.org/10.1029/2004JB003114

Kirschner, J. P., Kominz, M. A., & Mwakanyamale, K. E. (2010). Quantifying extension of passive margins: Implications for sea level change. *Tectonics*, *29*, TC4006. https://doi.org/10.1029/2009TC002557

Klinkmüller, M. (2011). *Properties of analogue materials, experimental reproducibility and 2D/3D deformation quantification techniques in analogue modeling of crustal-scale processes, (Doctoral dissertation)*. University of Bern.

Koyi, H. (1997). Analogue modelling: From a qualitative to a quantitative technique – A historical outline. *Journal of Petroleum Geology*, *20*(2), 223–238. https://doi.org/10.1111/j.1747-5457.1997.tb00774.x

Krýza, O., Závada, P., & Ondrej, L. (2019). Advanced strain and mass transfer analysis in crustal-scale oroclinal buckling and detachment folding analogue models. *Tectonophysics*, *764*, 88–109. https://doi.org/10.1016/j.tecto.2019.05.001

Lavier, L. L., & Manatschal, G. (2006). A mechanism to thin the continental lithosphere at magma-poor margins. *Nature*, *440*(7082), 324–328. https://doi.org/10.1038/nature04608

Le Calvez, J. H., & Vendeville, B. C. (2002). Experimental designs to model along-strike fault interaction. *Journal of the Virtual Explorer*, *7*, 1–17. https://doi.org/10.3809/jvirtex.2002.00043

Levell, B., Argent, J., Doré, A. G., & Fraser, S. (2010). Passive margins: Overview. *Geological Society, London, Petroleum Geology Conference Series*, *7*(1), 823–830. https://doi.org/10.1144/0070823

Luth, S., Willingshofer, E., Sokoutis, D., & Cloetingh, S. (2010). Analogue modelling of continental collision: Influence of plate coupling on mantle lithosphere subduction, crustal deformation and surface topography. *Tectonophysics*, *484*(1–4), 87–102. https://doi.org/10.1016/j.tecto.2009.08.043

Maestrelli, D., Montanari, D., Corti, G., Del Ventisette, C., Moratti, G., & Bonini, M. (2020). Exploring the interactions between rift propagation and inherited crustal fabrics through experimental modeling. *Tectonics*, *39*(12), e2020TC006211. https://doi.org/10.1029/2020TC006211

McClay, K. R. (1990). Extensional fault systems in sedimentary basins: A review of analogue model studies. *Marine and Petroleum Geology*, *7*(3), 206–233. https://doi.org/10.1016/0264-8172(90)90001-W

McClay, K. R. (1996). Recent advances in analogue modelling: Uses in section interpretation and validation. *Geological Society, London, Special Publication*, *99*(1), 201–225. https://doi.org/10.1144/GSL.SP.1996.099.01.16

McClay, K. R., & White, M. J. (1995). Analogue modelling of orthogonal and oblique rifting. *Marine and Petroleum Geology*, *12*(2), 137–151. https://doi.org/10.1016/0264-8172(95)92835-K

Michon, L., & Merle, O. (2000). Crustal structures of the Rhinegraben and the Massif Central grabens: An experimental approach. *Tectonics*, *19*(5), 896–904. https://doi.org/10.1029/2000TC900015

Michon, L., & Merle, O. (2003). Mode of lithospheric extension: Conceptual models from analogue modeling. *Tectonics*, *22*(4), 1028. https://doi.org/10.1029/2002TC001435

Molnar, N. E., Cruden, A. R., & Betts, P. G. (2017). Interactions between propagating rotational rifts and linear rheological heterogeneities: Insights from three-dimensional laboratory experiments. *Tectonics*, *36*(3), 420–443. https://doi.org/10.1002/2016TC004447

Molnar, N. E., Cruden, A. R., & Betts, P. G. (2018). Unzipping continents and the birth of microcontinents. *Geology*, *46*(5), 451–454. https://doi.org/10.1130/G40021.1

Mulugeta, G. (1988). Squeeze box in a centrifuge. *Tectonophysic*s, *148*(3–4), 323–335. https://doi.org/10.1016/0040-1951(88)90139-4

Nagel, T. J., & Buck, W. R. (2004). Symmetric alternative to asymmetric rifting models. *Geology*, *32*(11), 937–940. https://doi.org/10.1130/G20785.1

Naylor, M. A., Laroque, J. M., & Gauthier, B. D. M. (1994). Understanding extensional tectonics: Insights from sandbox models. Geodynamic evolution of sedimentary basin. International Symposium, Moscow (pp. 69–83).

Nestola, Y., Storti, F., Bedogni, E., & Cavozzi, C. (2013). Shape evolution and finite deformation pattern in analog experiments of lithosphere necking. *Geophysical Research Letters*, *40*(19), 5025–5057. https://doi.org/10.1002/grl.50978

Nestola, Y., Storti, F., & Cavozzi, C. (2015). Strain rate-dependent lithosphere rifting and necking architectures in analog experiments. *Journal of Geophysical Research: Solid Earth*, *120*(1), 584–594. https://doi.org/10.1002/2014JB011623

Oliveira, M. E., Gomes, A. S., Rosas, F. M., Duarte, J. M., França, G. S., Alemeida, J. C., & Fuck, R. A. (2022). 2D numerical modelling of double graben nucleation during early continental rifting: The role of crustal rheology and inherited mechanical weaknesses. *Tectonophysics*. https://doi.org/10.1016/j.tecto.2022.229281

Osagiede, E. E., Rosenau, M., Rotevatn, A., Gawthorpe, R., Jackson, C. A.-L., & Rudolf, M. (2021). Influence of zones of pre-existing crustal weakness on strain localization and partitioning during rifting: Insights from analog modeling using high-resolution 3D digital image correlation. *Tectonics*, *40*(10), e2021TC006970. https://doi.org/10.1029/2021TC006970

Panien, M., Buiter, S. J. H., Schreurs, G., & Pfiffner, O. A. (2006). Inversion of a symmetric basin: Insights from a comparison between analogue and numerical experiments. *Geological Society, London, Special Publicaitons*, *253*(1), 253–270. https://doi.org/10.1144/GSL.SP.2006.253.01.13

Péron-Pinvidic, G., & Manatschal, G. (2010). From microcontinents to extensional allochthons: Witnesses of how continents rift and break apart? *Petroleum Geoscience*, *16*(3), 189–197. https://doi.org/10.1144/1354-079309-903

Poppe, S., Holohan, E. P., Galland, O., Buls, N., Van Gompel, G., Keelson, B., et al. (2019). An inside perspective on magma intrusion: Quantifying 3D displacement and strain in laboratory experiments by dynamic X-ray computed tomography. *Frontiers in Earth Sciences*, *7*, 62. https://doi.org/10.3389/feart.2019.00062

Ramberg, H. (1981). *Gravity, deformation and the Earth's crust*. Academic Press.

Rudolf, M., Boutelier, D., Rosenau, M., Schreurs, G., & Oncken, O. (2016). Rheological benchmark of silicone oils used for analog modeling of short- and long-term lithospheric deformation. *Tectonophysics*, *684*, 12–22. https://doi.org/10.1016/j.tecto.2015.11.028

Samsu, A., Cruden, A. R., Molnar, N. E., & Weinberg, R. F. (2021). Inheritance of penetrative basement anisotropies by extension-oblique faults: Insights from analogue experiments. *Tectonics*, *40*(5), e2020TC006596. https://doi.org/10.1029/2020TC006596

Saria, E., Calais, E., Stamps, D. S., Delvaux, D., & Hartnady, C. J. H. (2014). Present-day kinematics of the East African Rift. *Journal of Geophysical Research: Solid Earth*, *119*(4), 3584–3600. https://doi.org/10.1002/2013JB010901

Sassi, W., Colletta, B., Balé, P., & Paquereau, T. (1993). Modelling of structural complexity in sedimentary basins: The role of pre-existing faults in thrust tectonics. *Tectonophysics*, *226*(1–4), 97–112. https://doi.org/10.1016/0040-1951(93)90113-X

Schmid, T. C., Schreurs, G., & Adam, J. (2022a). Characteristics of continental rifting in rotational systems: New findings from spatiotemporal high resolution quantified crustal scale analogue models. *Tectonophysics*, *822*, 229174. https://doi.org/10.1016/j.tecto.2021.229174

Schmid, T. C., Schreurs, G., & Adam, J. (2022b). Rotational extension promotes coeval upper crustal brittle faulting and deep-seated rift-axis parallel flow: Dynamic coupling processes inferred from analog model experiments. *Journal of Geophysical Research: Solid Earth*, *127*(8), e2022JB024434. https://doi.org/10.1029/2022JB024434

Schmid, T., Zwaan, F., Corbi, F., Funiciello, F., & Schreurs, G. (2022c). Rheology of glucose syrup from the Tectonic Modelling Lab (TecLab) of the University of Bern (CH). *GFZ Data Services*. https://doi.org/10.5880/fidgeo.2022.030

Schori, M., Zwaan, F., Schreurs, G., & Mosar, J. (2021). Pre-existing basement faults controlling deformation in the Jura Mountains fold-and-thrust belt: Insights from analogue models. *Tectonophysics*, *814*, 228980. https://doi.org/10.1016/j.tecto.2021.228980

Schreurs, G., Buiter, S. J. H., Boutelier, D., Burberry, C., Callot, J.-P., Cavozzi, C., et al. (2016). Benchmarking analogue models of brittle thrust wedges. *Journal of Structural Geology*, *92*, 116–139. https://doi.org/10.1016/j.jsg.2016.03.005

Schreurs, G., Buiter, S. J. H., Boutelier, D., Corti, G., Costa, E., Cruden, A. R., et al. (2006). Analogue benchmarks of shortening and extension experiments. *Geological Society, London, Special Publications*, *253*, 1–27. https://doi.org/10.1144/GSL.SP.2006.253.01.01

Schreurs, G., Hänni, R., Panien, M., & Vock, P. (2003). Analysis of analogue models by helical X-ray computed tomography. *Geological Society, London, Special Publications*, *215*(1), 213–223. https://doi.org/10.1144/GSL.SP.2003.215.01.20

Smith, N. J. P., Shepherd, T. J., Styles, M. T., & Williams, G. M. (2005). Hydrogen exploration: A review of global hydrogen accumulations and implications for prospective areas in NW Europe. *Geological Society, London, Petroleum Geology Conference Series*, *6*(1), 349–358. https://doi.org/10.1144/0060349

Sokoutis, D., & Willingshofer, E. (2011). Decoupling during continental collision and intra-plate deformation. *Earth and Planetary Science Letters*, *305*(3–4), 435–444. https://doi.org/10.1016/j.epsl.2011.03.028

Sun, Z., Zhong, Z., Keep, M., Zhou, D., Cai, D., Li, X., et al. (2009). 3D analogue modeling of the South China sea: A discussion on breakup pattern. *Journal of Asian Earth Sciences*, *34*(4), 544–556. https://doi.org/10.1016/j.jseaes.2008.09.002

Tron, B., & Brun, J.-P. (1991). Experiments on oblique rifting in brittle-ductile systems. *Tectonophysics*, *188*(1–2), 71–84. https://doi.org/10.1016/0040-1951(91)90315-J

Vendeville, B., Cobbold, P. R., Davy, P., Choukroune, P., & Brun, J. P. (1987). Physical models of extensional tectonics at various scales. *Geological Society, London, Special Publications*, *28*(1), 95–107. https://doi.org/10.1144/GSL.SP.1987.028.01.08

Warsitzka, M., Ge, Z., Schönebeck, J.-M., Pohlenz, A., & Kukowski, N. (2019). Ring-shear test data of foam glass beads used for analogue experiments in the Helmholtz Laboratory for Tectonic Modelling (HelTec) at the GFZ German Research Centre for Geosciences in Potsdam and the Institute of Geosciences, Friedrich Schiller University Jena. *GFZ Data Services*. https://doi.org/10.5880/GFZ.4.1.2019.002

Weijermars, R., & Schmeling, H. (1986). Scaling of Newtonian and non-Newtonian fluid dynamics without inertia for quantitative modelling of rock flow due to gravity (including the concept of rheological similarity). *Physics of the Earth and Planetary Interiors*, *43*(4), 316–330. https://doi.org/10.1016/0031-9201(86)90021-x

Willingshofer, E., & Sokoutis, D. (2009). Decoupling along plate boundaries: Key variable controlling the mode of deformation and the geometry of collisional mountain belts. *Geology*, *37*(1), 39–42. https://doi.org/10.1130/G25321A.1

Willingshofer, E., Sokoutis, D., Beekman, F., Schönebeck, J.-M., Warsitzka, M., & Rosenau, M. (2018). Ring shear test data of feldspar sand and quartz sand used in the Tectonic Laboratory (TecLab) at Utrecht University for experimental Earth Science applications. V. 1. *GFZ Data Services*. https://doi.org/10.5880/fidgeo.2018.072

Willingshofer, E., Sokoutis, D., Luth, S. W., Beekman, F., & Cloetingh, S. (2013). Subduction and deformation of the continental lithosphere in response to plate and crust-mantle coupling. *Geology*, *41*(12), 1239–1242. https://doi.org/10.1130/G34815.1

Wilson, J. T. (1966). Did the Atlantic close and then re-open? *Nature*, *211*(5050), 676–681. https://doi.org/10.1038/211676a0

Wilson, R. W., Houseman, G. A., Buiter, S. J. H., McAffrey, K. J. W., & Doré, A. G. (2019). Fifty years of the Wilson Cycle concept in plate tectonics: An overview. *Geological Society, London, Special Publications*, *470*, 1–17. https://doi.org/10.1144/SP470-2019-58

Withjack, M. O., & Jamison, W. R. (1986). Deformation produced by oblique rifts. *Tectonophysics*, *126*(2–4), 99–124. https://doi.org/10.1016/0040-1951(86)90222-2

Zou, C., Zhai, G., Zhang, G., Wang, H., Zhang, G., Li, J., et al. (2015). Formation, distribution, potential and prediction of global conventional and unconventional hydrocarbon resources. *Petroleum Exploration and Development*, *42*(1), 14–28. https://doi.org/10.1016/S1876-3804(15)60002-7

Zwaan, F. (2017). *4D laboratory experiments of oblique extension and scissor tectonics, structural inheritance and sedimentation: Implications for rift evolution, rift propagation and rift segment interaction, (Doctoral dissertation)*. University of Bern. Retrieved from BORIS repository https://boristheses.unibe.ch/824/

Zwaan, F., Chenin, P., Erratt, D., Manatschal, G., & Schreurs, G. (2021). Complex rift patterns, a result of interacting crustal and mantle weaknesses, or multiphase rifting? Insights from analogue models. *Solid Earth*, *12*(7), 1473–1495. https://doi.org/10.5194/se-12-1473-2021

Zwaan, F., Chenin, P., Erratt, D., Manatschal, G., & Schreurs, G. (2022). Competition between 3D structural inheritance and kinematics during rifting: Insights from analogue models. *Basin Research*, *34*(2), 824–854. https://doi.org/10.1111/bre.12642

Zwaan, F., & Schreurs, G. (2022). Analogue modelling of continental rifting: An overview. In G. Peron-Pinvidic (Ed.), Rifted Margins, ISTE-WILEY. https://doi.org/10.1002/9781119986928.ch6

Zwaan, F., & Schreurs, G. (2023a). Digital image correlation (DIC) and X-Ray CT analyses of lithospheric-scale analogue models of continental rifting. *GFZ Data Services*. https://doi.org/10.5880/fidgeo.2023.006

Zwaan, F., & Schreurs, G. (2023b). A novel method for analogue modelling of lithospheric-scale rifting, monitored via X-ray CT-scanning methods, at the University of Bern Tectonic Modelling Lab (CH). *GFZ Data Services*. https://doi.org/10.5880/fidgeo.2023.005

Zwaan, F., Schreurs, G., & Adam, J. (2018). Effects of sedimentation on rift segment evolution and rift interaction in orthogonal and oblique extensional settings: Insights from analogue models analysed with 4D X-ray computed tomography and digital volume correlation techniques. *Global and Planetary Change*, *171*, 110–133. https://doi.org/10.1016/j.gloplacha.2017.11.002

Zwaan, F., Schreurs, G., & Buiter, S. J. H. (2019). A systematic comparison of experimental set-ups for modelling extensional tectonics. *Solid Earth*, *10*(4), 1063–1097. https://doi.org/10.5194/se-10-1063-2019

Zwaan, F., Schreurs, G., Naliboff, J., & Buiter, S. J. H. (2016). Insights into the effects of oblique extension on continental rift interaction from 3D analogue and numerical models. *Tectonophysics*, *693*, 239–260. https://doi.org/10.1016/j.tecto.2016.02.036

Zwaan, F., Schreurs, G., Ritter, M., Santimano, T., & Rosenau, M. (2018). Rheology of PDMS-corundum sand mixtures from the tectonic modelling lab of the University of Bern (CH). V. 1. *GFZ Data Services*. https://doi.org/10.5880/fidgeo.2018.023

Zwaan, F., Schreurs, G., & Rosenau, M. (2020). Rift propagation in rotational versus orthogonal extension: Insights from 4D analogue models. *Journal of Structural Geology*, *135*, 103946. https://doi.org/10.1016/j.jsg.2019.103946

Zwaan, F., Schreurs, G., Rudolf, M., & Rosenau, M. (2022). Ring-shear test data of feldspar FS900S used in the Tectonic Modelling Laboratory at the University of Bern (Switzerland). *GFZ Data Services*. https://doi.org/10.5880/fidgeo.2022.008